WILEY-VCH

DOI: 10.1002/
Article type: Full Paper

A New Approach to Stable Cationic and Anionic Redox Activity in O3-Layered Cathode for Sodium-Ion Batteries

Natalia Voronina,[a] Najma Yaqoob,[b] Hee Jae Kim,[a] Kug-Seung Lee,[c] Hee-Dae Lim,[d] Hun-Gi Jung,[d] Olivier Guillon,[b] Payam Kaghazchi,[b],* *Seung-Taek Myung*[a],*

[a]*Hybrid Materials Research Center, Department of Nano Technology and Advanced Materials Engineering, Sejong Battery Institute, Sejong University, Seoul, 05006, South Korea*

[b]*Forschungszentrum Jülich GmbH, Institute of Energy and Climate Research, Materials Synthesis and Processing (IEK-1), Jülich, Germany*

[c]*Pohang Accelerator Laboratory, 80 Jigokro-127-beongil, Nam-gu, Pohang, Gyeongbuk 37673, South Korea*

[d]*Center for Energy Storage Research, Korea Institute of Science and Technology, Seoul, 02792, South Korea*

E-mail: p.kaghazchi@fz-juelich.de (P. Kaghazchi)
E-mail: smyung@sejong.ac.kr (S. Myung)

Keywords: Cathode; Cationic; Anionic; Redox; Sodium; Battery.

Abstract

Herein, we reveal the stable cationic and anionic redox in an O3-type layered $Na[Ni_{2/3}Ru_{1/3}]O_2$ cathode for sodium-ion batteries (SIBs). Density functional theory (DFT) calculation shows that the electron density features change in density of state with mixing of delocalized valence states as well as localized deeper energy states of O(*p*), Ni(*d*), and Ru(*d*) for the highly desodiated $Na_{1-x}[Ni_{2/3}Ru_{1/3}]O_2$ electrode, revealing the covalent characteristic of the transition metal (TM)–O and TM–TM bonds in the charged system. These properties lead to cycling stability for 200 cycles, with approximately 79% of the capacity retained at a rate of 1C (210 mA g^{-1}). *Operando* X-ray diffraction, X-ray absorption spectroscopy, and DFT calculations reveal the reversible electrochemical activity of the Ni^{2+}/Ni^{3+} and O^{2-}/O^{1-} redox reactions, which are sustainable throughout the cycles. In addition, no loss of oxygen from the crystal structure of $Na[Ni_{2/3}Ru_{1/3}]O_2$ occurs according to differential electrochemical mass spectrometry. Our findings provide additional insight into the complex mechanism of the oxygen redox activity of high-capacity O3-type cathode materials for SIBs, encouraging further studies on their development.

1. Introduction

Anion redox-active centers in transition-metal oxides play a critical role in the development of high-energy-density cathodes for lithium-ion and sodium-ion batteries (LIBs and SIBs, respectively).[1-6] Recently, the capacity of LIBs has been shown to depend not only on the transition-metal redox but also on the anion redox, such as sulfur redox[7-9] or oxygen redox [10,11]. Anionic redox can contribute additional capacity, thereby increasing the energy density of the battery. This phenomenon has been observed in over-stoichiometric lithium compounds, where lithium partially replaces transition metals (TMs) with typical features of $Li[Li_xTM_{1-x}]O_2$ (TM=Ni, Co, Fe, Cu, etc.)[12-14] or $Li_{1+x}TM_{1-x}O_2$(TM= Ru, Ir)[15,16]. These materials deliver higher capacity than the theoretical capacity derived from the TM redox couple. The former compounds, based on a 3*d* (Mn) metal, are of interest because of their high capacity exceeding 250 mAh (g-oxide)$^{-1}$, reasonable prices, and available resources. However, they still suffer from voltage decay and irreversible capacity fading, associated with cation migration in the crystal lattice and oxygen release during the charging process.[12,17,18] The latter compounds, based on 4*d* (Ru) and 5*d* (Ir) noble metals, have attracted significant attention from fundamental and theoretical points of view. It has been established that moving from 3*d* (Mn) to 4*d* (Ru) or 5*d* (Ir) metals can increase the TM–O covalence and stabilize the oxygen-redox reactions.[19-21] Such higher covalence enhances the structural rigidity and reduces the stress associated with removal of lithium ions from the structure.[22]

For SIBs, the anionic redox reaction is available for not only Na-rich materials but also Na-deficient P2/P3-type compounds.[23-35] For example, manganese-based P2-type sodium-deficient materials with low-valence substituents, such as Li,[26,30,31] Zn,[23,29] and Mg,[27,28] have demonstrated oxygen-redox activity with good structural stability. It is generally accepted that a Na-O-A (A=Li, Na, Mg, Zn or vacancy) local coordination environment is the essential requirement for oxygen redox activation in P2/O3 type layered $Na_x[ATM]O_2$ (TM: transition metals).[23-51] The presence of the Na–O–A configuration triggers anionic reactions, which are dependent on the structures through irreversible O_2 evolution, reversible redox, and hysteresis process. Migration of those Li and Na in the transition metal layers toward Na layers induces formation of lone pair electrons in O 2*p* orbital, such that the high density of state energy for oxygen allows oxidation of oxygen although the reaction occurs kinetically sluggish. Recent progress has enabled the sluggish kinetics of oxygen-redox and low energy density caused by the low voltage of the Mn^{4+}/Mn^{3+} redox couple to be circumvented; specifically, covalence between O *2p* and Cu *3d,*[32,33] Ni *3d,*[24] or Co *3d*[25,35] substantially promotes facile electron transfer and increases in operation voltage and provides reversibility of the oxygen-redox reaction, proved in sodium-deficient P2-type $Na_{2/3}[Ni_{1/3}Mn_{2/3}]O_2$[36] and $Na_{2/3}[Cu_{0.28}Mn_{0.72}]O_2$[37] without such Na-O-A local configuration. Density functional theory (DFT) calculation and mapping of resonant inelastic X-ray scattering (mRIXS) demonstrated that the reversible oxygen redox could take place due to a higher covalence of Ni-O and Cu-O bonds at highest desodiated states, which leads to the energy of O *2p* in e_g* (Ni-O/Cu-O) becomes higher than that of Ni 3*d*/Cu 3*d*, which, therefore, facilitates the oxygen redox reaction.

The possibility of using Na-rich materials with the formula Na_2TMO_3 (*TM*: Ru or Ir) has recently been proposed by the groups of Yamada[38,39] and Tarascon[40,41]. Interestingly, these Na-rich materials also exhibit reversible extra capacity induced by oxygen redox, exceeding 1 mol Na^+ per formula unit. Yamada et al. demonstrated that the honeycomb-structured Na_2RuO_3 invokes the oxygen-redox reaction (O^{2-}/O^{1-}) after the cationic redox reaction (Ru^{4+}/Ru^{5+}).[38] Further investigation of the solid-solution family $Na_2Ru_{1-y}Sn_yO_3$ (y = 0 to 0.75) revealed that the cumulative cationic Ru^{4+}/Ru^{5+} and anionic O^{2-}/O^{1-} redox reactions were involved in the charge compensation process.[40] The O3-type Ru-based $Na[Mg_{2/3}Ru^{4+}{}_{1/3}]O_2$ and $Na[Mg_{1/2}Ru^{5+}{}_{1/2}]O_2$ were electrochemically active achieved by oxygen-redox, accompanied by sluggish kinetics without O_2 loss.[42] Recently, Zhou et al.[43] reported that a superlattice-stabilized O3-type $Na[Ni_{2/3}Ru_{1/3}]O_2$, showing only cationic Ni^{2+}/Ni^{3+} redox was responsible for charge compensation with limited capacity of about 130 mAh g^{-1} in the voltage range of 2-3.8 V. The above works highlight feasibility of Ru-based cathode materials with reasonable capacity and retention.

We approach that increasing covalency in the structure could endorse to realize the activation of oxygen redox couple. Considering Pauling electronegativity of Ru (2.2), which is higher than Ni (1.91), Zn (1.65) or Mg (1.33), might induce Ru–O bonds more covalent so that electrons are inclined to delocalize on the ruthenium cations and oxygen anions[36,37]; namely, overlapping of Ru 4*d* with the O 2*p* orbitals may generate not only the cumulative transition metal redox but also the reversible charge compensation progressed by oxygen redox. In this work, we introduce the unique behavior of layered O3 type $Na[Ni_{2/3}Ru_{1/3}]O_2$, exhibits a reversible capacity of 154 mAh (g-oxide)$^{-1}$ that is associated with both cationic Ni^{3+}/Ni^{2+} and anionic O^{2-}/O^{1-} redox pairs, for which the anionic behavior is related to an additional phase transition to the O1 phase, as observed by *operando* X-ray diffraction (*o*-XRD). Although Ru was inactive during the electrochemical reaction, the oxidation of oxygen affects its local environment in RuO_6 octahedra such that the Ru–O distance is reduced on charge (oxidation) and recovers during discharge (reduction), as confirmed by X-ray absorption spectroscopy and first-principles calculation. It is evident that the combination of 3*d* and 4*d* TMs is responsible for the high capacity and stable cycling performance owing to the presence of high covalence in the structure. Oxygen redox offers the additional benefit of increasing the capacity derived from the 4*d* TM. Herein, we unveil the highly stable cationic and anionic redox activity in the O3-type layered $Na[Ni_{2/3}Ru_{1/3}]O_2$ compound for sodium storage using experiments and theoretical calculations.

2. Results and Discussion

Rietveld refinement of the X-ray diffraction (XRD) data for $Na[Ni_{2/3}Ru_{1/3}]O_2$ was performed using the hexagonal O3 phase ($R\bar{3}m$) (**Figure 1a** and **Table S1**). For the refinement, we confirmed the atomic ratio of Na:Ni:Ru to be 1.00:0.67:0.33 using inductively coupled plasma-atomic emission spectroscopy (ICP-AES). The XRD data indicated that the Na and Ni/Ru atoms were alternatively distributed within the oxygen framework stacked along the *c* direction with the ABCABC sequence (**Figure 1a inset**). The calculated lattice parameters were $a = 3.0310(9)$ Å and $c = 15.9353(9)$ Å, which are consistent with the results reported by Zhou et al.[47] Scanning electron microscopy (SEM) analysis showed that the $Na[Ni_{2/3}Ru_{1/3}]O_2$ was composed of uniform primary particles with sizes in the range of 0.5–2 μm (**Figure S1**). Transmission electron microscopy (TEM) and the corresponding selected-area electron diffraction pattern (SAED) confirmed that the designed structure possessed hexagonal symmetry (**Figure 1b**). Energy-dispersive X-ray spectrometry (EDX) mappings showed that Na, Ni, Ru, and O were uniformly distributed in the particles (**Figure 1b-1–1b-4**). The average oxidation state of Ni was similar to that of the reference, $Li[Ni_{1/3}Co_{1/3}Mn_{1/3}]O_2$ with Ni^{2+}, according to the X-ray absorption near-edge structure spectroscopy (XANES) (**Figure 1c**). Emergence of a shoulder in the pre-edge is generally observed at approximately 22,120 keV with the presence of Ru^{4+} in the compound (**Figure 1c**). Compared with RuO_2, $Na[Ni_{2/3}Ru_{1/3}]O_2$ did not show the pre-edge in the Ru K-edge spectrum, indicating that Ru is stabilized as 5+ (**Figure 1d**). These values are expected for achieving a total charge balance in the compound assuming that the oxidation states of O and Na are 2- and 1+, respectively.

The cycling performance of $Na[Ni_{2/3}Ru_{1/3}]O_2$ was investigated in galvanostatic mode between 2 and 4.1 V at a current of 10.5 mA g^{-1} (0.05C) (**Figure 2a**). The electrode delivered a first charge (oxidation) capacity of ~165 mAh g^{-1}, which is consistent with ~0.79 mol Na^+ extraction from the formula unit. The first charge curve consisted of two plateaus at 3 and 3.05 V, followed by a sloppy curve up to 3.8 V and a third plateau at 3.9 V (**Figure 2a and 2b**). During discharge (reduction), the reaction was reversible with three voltage plateaus at 3.5, 3, and 2.95 V, providing a discharge capacity of 154 mAh g^{-1}. In consideration of the GITT results with the open circuit voltages (OCV) at equilibrium states (**Figure S2**), it was able to observe the reversible voltage plateau at 3.9/3.5 V at first and second charge/discharge, respectively, despite the plateau becoming shorter on the second charge. Delivered capacity was approximately 125 mAh g^{-1} at the 100th cycle, retaining approximately 81% of the first discharge capacity (**Figure 2c**). In addition, although the capacity somewhat declined to 117 mAh g^{-1} at a rate of 1C (210 mA g^{-1}) (**Figures 2d and 2e**), the corresponding capacity retention was approximately 79% of the first capacity after 200 cycles (**Figure 2f**). The $Na[Ni_{2/3}Ru_{1/3}]O_2$ electrode was able to show its activity even at 10C (2.1 A g^{-1}), delivering approximately 65 mAh g^{-1} (**Figures 2d and 2e**).

Operando X-ray diffraction (*o*-XRD) analysis revealed the successive phase transitions of $Na[Ni_{2/3}Ru_{1/3}]O_2$ (**Figure 3a**) measured along the voltage profile (**Figure 3b**). In the early stage of desodiation to $x = 0.125$ in $Na_{1-x}[Ni_{1/2}Ru_{1/3}]O_2$, the (003) and (006) peaks at 16.7° and 33.8° (2θ), respectively, shifted toward lower angles, whereas the (001) and (012) peaks at 34.6° and 36.1° (2θ), respectively, moved to higher angles (**Figure 3a**). The relative intensity of the $Na[Ni_{1/2}Ru_{1/3}]O_2$ phase started to decrease from $x = 0.125$ in $Na_{1-x}[Ni_{1/2}Ru_{1/3}]O_2$; however, new peaks emerged at 16.3°, 32.9°, 35.1° (2θ), attributed to the formation of the Na-deficient monoclinic O'3-type phase, which correlates with the first dQ/dV peak at approximately 3 V (**Figure 2b**). Further desodiation from $x = 0.225$ in $Na_{1-x}[Ni_{1/2}Ru_{1/3}]O_2$ resulted in the appearance of a second new series of peaks at 16.0°, 32.4°, and 35.4° (2θ) assigned as the monoclinic O"3-type sodium-deficient phase, corresponding to the second dQ/dV peak at approximately 3.05 V (**Figure 2b**). The new O'3 and O"3 phases are the distorted O-type phases due to the splitting of the (104) peak of the O3 phase into (-202) and (111) in the monoclinic system. Interestingly, the calculated lattice parameters gradually changed as desodiation progressed, although the biphasic reactions of O3–O'3 and O'3–O"3 governed in this range (**Figure 3c**). This successive formation of the monoclinic O'3 phase is the result of the continuous decrease in the β angle in the monoclinic structure as desodiation progressed, triggering the formation of a different structural system. From $x = 0.35$ in $Na_{1-x}[Ni_{1/2}Ru_{1/3}]O_2$

(> 3.2 V), a third series of peaks arose at 15.8°, 31.9°, 35.6°, 36.8°, and 44.7° (2θ), which belong to the hexagonal P3-type structure indexed as $(003)_{P3}$, $(006)_{P3}$, $(101)_{P3}$, $(012)_{P3}$, and $(015)_{P3}$, respectively. The P3-type structure, different from the O3 phase with an oxygen array of ABCABC sequence, has typical features of the oxygen layers stacking following an ABBCCA stacking sequence and the Na^+ ions occupying the prismatic sites sharing faces and edges with the surrounding TMO_6 octahedra. The monotonous peak shifting in $Na_{1-x}[Ni_{1/2}Ru_{1/3}]O_2$ ($0.38 \leq x \leq 0.65$) indicates that topotactic Na^+ extraction predominantly occurred *via* a single-phase reaction; namely, the Na slab spacing gradually expanded until the cell voltage increased to 3.8 V, $x = 0.675$ in $Na_{1-x}[Ni_{1/2}Ru_{1/3}]O_2$. Raising the voltage above 3.8 V led to the disappearance of the P3 phase. In addition, a new phase with peaks emerging at 35.7°, 38.5°, and 48.2° (2θ) was indexed as an O1-type phase with ABBA oxygen stacking in the range of $0.65 \leq x \leq 0.79$ in $Na_{1-x}[Ni_{1/2}Ru_{1/3}]O_2$. This new phase showed ΔV = ~1.4% and ~2.9% shrinkage in the unit-cell volume compared with that of the P3 and pristine O3 phases, respectively (**Figure 3d**). Therefore, the O3-$Na[Ni_{2/3}Ru_{1/3}]O_2$ delivered the charge capacity of 165 mAh g^{-1} *via* the above-mentioned multiple phase transition of O3–O'3–O"3–P3–O1, extracting 0.79 mol of Na^+ ions from $Na[Ni_{2/3}Ru_{1/3}]O_2$.

Upon discharge, the charged O1-$Na_{0.21}[Ni_{2/3}Ru_{1/3}]O_2$ phase first recovered to P3-$Na_{0.67}[Ni_{2/3}Ru_{1/3}]O_2$ and finally to the original O3-$Na_{0.94}[Ni_{2/3}Ru_{1/3}]O_2$ (**Figure 3a**), indicating the reversibility of the Na^+ insertion process following the phase-transition sequence of O1–P3–O"3–O'3–O3 in the $Na[Ni_{2/3}Ru_{1/3}]O_2$ electrode. Therefore, in the presence of high covalence in the structure, the suggested reversible phase transitions with small variation in the volume offer a possible explanation for the long-term cycling stability, as shown in **Figure 2**. It is noteworthy that the same reversible sequences of phase transitions, namely O3–O'3–O"3–P3–O1 on charge and O1–P3–O"3–O'3–O3 on discharge, appeared during the second and third cycles (**Figure S3**).

The local structural changes of Ni, Ru, and O in the Na[$Ni_{2/3}Ru_{1/3}$]O_2 electrode were investigated using XANES and X-ray photoelectron spectroscopy (XPS) during the first charge and discharge (**Figure 4**). The Ni K-edge shifted toward higher photon energy during the entire charging process (**Figure 4a**). Upon charging, the Ni K-edge shifted close to the Li[$Ni_{0.8}Co_{0.1}Mn_{0.1}$]O_2 reference with Ni^{3+}. On discharge, the Ni K-edge spectrum returned to the initial state, indicating that the oxidized Ni^{3+} was reversibly reduced to Ni^{2+}. The variation in the Ni–O distance in the extended X-ray absorption fine structure (EXAFS) provides evidence of the $Ni^{2+/3+}$ redox pair (**Figure 4b**). Based on the $Ni^{2+/3+}$ redox reaction, the capacity achieved by the Ni redox was calculated to be 140 mAh g^{-1}.

An unusual change was observed in the Ru K-edge spectra on charge (**Figure 4c**). The oxidation state of Ru in Na[$Ni_{2/3}Ru_{1/3}$]O_2 is 5+, such that further oxidation is not possible in the operation range of 2–4.1 V. It is evident that except for the emergence in the pre-edge at the end of charge, O1-$Na_{0.21}$[$Ni_{2/3}Ru_{1/3}$]O_2, the Ru K-edge did not change on charge. The reverse tendency was observed on discharge, namely, the pre-edge was not perceived at the end of discharge, O3-$Na_{0.94}$Na[$Ni_{2/3}Ru_{1/3}$]O_2. The EXAFS data revealed no change in the Ru–O distances on charge and *vice versa* on discharge (**Figure 4d**); however, the distances varied in the Ru–Ru/Ni shell, which is associated with the neighboring $Ni^{2+/3+}$ redox reaction, reflecting the local structural change. These phenomena are consistent with the results for Ru-based Li-rich compounds studied by Tarascon et al.[44] and Cabana et al.[45], demonstrating that the hybridization between Ru 5*p* and 4*d* states is enhanced in a distorted octahedral coordination, increasing the pre-edge peak. Furthermore, we observed Ru 3*p* XPS spectra for the first cycle to prove the inactivity of Ru in Na[$Ni_{2/3}Ru_{1/3}$]O_2 in the voltage range 2-4.1 V (**Figure S4**). The results showed that the fresh material presented Ru 3$p_{3/2}$ and Ru 3$p_{1/2}$ core peaks at 465 eV and 487 eV, respectively, corresponding to the Ru^{5+}-O binding energy. Upon charging and discharging, no shifts were observed in the binding energy in the whole range. This finding is consistent with the XANES (**Figure 4c**) and EXAFS (**Figure 4d**) data that Ru was retained its valance state constantly as 5+ during the first cycle in the voltage range 2-4.1 V, agreeing with the data reported by Zhou et al.[43,46] Moreover, we tested the present $Na[Ni_{2/3}Ru_{1/3}]O_2$ electrode in the voltage range of 0-4.1 V (**Figure S5**); namely, it did not show Ru^{5+}/Ru^{4+} couple even to 0 V discharge, proving inactivity of Ru in $Na[Ni_{2/3}Ru_{1/3}]O_2$.

In addition, the valence of Ru is dependent on the chemical composition. In our case of O3 type $Na[Ni_{2/3}Ru_{1/3}]O_2$, Ni is divalent, so that Ru is spontaneously stabilized as 5+. Otherwise, assuming that Ru is stabilized as Ru^{4+}, the average oxidation state of Ni becomes 2.5+. However, our XANES data demonstrated that Ni suited as Ni^{2+} in **Figure 1c**. Also, the absence of pre-edge peak for the present $Na[Ni_{2/3}Ru_{1/3}]O_2$ is the evidence of Ru valence as 5+ in **Figure 1d**, which will be further mentioned in DFT calculations (**Figure 7 and 8**). Again, not all but some of Ru in O3 and P2 type layered oxides are stabilized as 4+. Also, some of Ru in P2 and O3 type layered compounds cathodes where Ru are stabilized as 5+. For example, in the work of Zhou et al.[51] in O3-Na_3RuO_4 ($C2/m$) Ru was stabilized as 5+ and did not participate in the electrochemical reaction. Similar feature was also observed in the works of $Na[Mg_{2/3}Ru_{1/3}]O_2$[42] and $Na[Ni_{2/3}Ru_{1/3}]O_2$[43], where Ru was stabilized as 5+; however, depending on the neighboring environment was electroactive Ru^{4+}/Ru^{5+} and non- electroactive Ru^{5+}, respectively. Therefore, it is concluded that the average oxidation state of Ru may vary from 4+ to 5+ depending on structure and chemical composition, and Ru can be electroactive and non-electroactive regardless of its initial oxidation state (**Table S2**).[34,42,43,46-49]

Turning to the oxygen redox activity in this material, the O K-edge spectrum was measured and XPS analysis was performed for $Na[Ni_{2/3}Ru_{1/3}]O_2$ (**Figure 4e and f**). Two peaks appeared in the O K-edge XANES spectrum at approximately 529.6 and 530.7 eV, corresponding to the TM $3d/4d$–O$2p$ t_{2g} and e_g hybridized states, respectively (**Figure 4e**). Charging the $Na[Ni_{2/3}Ru_{1/3}]O_2$ electrode to 3.2 V clearly resulted in an increase in the intensity of the t_{2g} peak at 529.6 eV but a decrease in the e_g peak at 530.7 eV. Further charging to 4.1 V resulted in two interesting features in those orbitals, namely, broadening and development of the intensity at 529.6 V and disappearance of the peak at 530.7 eV. This change in the O K-edge resulted from the oxidation of oxygen in $Na[Ni_{2/3}Ru_{1/3}]O_2$ from O^{2-} toward O^{1-} on charge. During discharge to 2 V, the reverse process occurred with lowering of the intensity of the peak at 529.6 eV peak and recovery of the peak at 530.7 eV. This tendency was further revealed in the *ex situ* O 1*s* XPS spectrum (**Figure 4f**), which showed three peaks at 529.6 eV (lattice oxygen, O^{2-}), 530.2 eV (lattice oxygen O^{n-}_2, $n < 2$), and 532.7 eV (electrolyte oxidation). After charging to 3.2 V, no obvious changes in the peak locations or areas were observed. However, after charging to 4.1 V, a new shoulder appeared at approximately 530.2 eV, which is attributed to the oxidation of O^{2-} to peroxo-like dimers (O^{n-}_2). In addition, the peroxo-related peak was still visible during discharge to 3 V and disappeared at 2 V, meaning that the oxidized lattice oxygen was reduced to O^{2-} in the $Na[Ni_{2/3}Ru_{1/3}]O_2$. As mentioned in **Figures 4c and 4d**, the distortion of RuO_6, observed from growth of the Ru pre-edge, is related to the oxidation of oxygen, which will be mentioned in the density functional theory (DFT) calculations (**Figures 7 and 8**). This finding in the O K-edge and XPS data verify the reversible activity of the O^{2-}/O^{1-} oxygen redox in $Na[Ni_{2/3}Ru_{1/3}]O_2$. In consideration of the delivered capacity (**Figure 2a**) and XAS (**Figure 4**) data, the capacity contributed by the O^{2-}/O^{1-} oxygen redox is approximately 25 mAh g^{-1} and is dominant in O1 phase region.

To confirm the availability of both cationic and anionic charge-compensation mechanisms in $Na[Ni_{2/3}Ru_{1/3}]O_2$ during a more convoluted cycle, we performed *ex situ* XANES measurements for the Ni, Ru, and O K-edge regions at the 50th cycle (**Figure 5**). Similar tendencies were observed at the 1st and 50th cycles for the Ni, Ru, and O K-edge spectra, indicating that not only the Ni^{3+}/Ni^{2+} redox couple but also oxygen-redox activities are highly stable and reversible for prolonged cycles in the $Na[Ni_{2/3}Ru_{1/3}]O_2$ electrode.

Because high covalence usually appears in 4*d* TMs, it was hypothesized that partial electron sharing between d_{Ru}, p_O, and d_{Ni} orbitals can induce such stable charge compensation of $Na[Ni_{2/3}Ru_{1/3}]O_2$. DFT calculation was thus performed to understand the detailed electronic configuration of $Na_x[Ni_{2/3}Ru_{1/3}]O_2$. To determine the arrangement of Ni and Ru cations in O3-$Na_9Ni_6Ru_3O_{18}$, we calculated the total Coulomb energies (E_c) for all the possible combinations of 6 Ni^{2+} and 3 Ru^{5+} in the 9 TM sites, namely $\frac{9!}{6!3!} = 84$. The charge states of Na and O were considered to be 1+ and 2−, respectively. The structure with the lowest E_c value was considered for DFT calculation. A similar arrangement of Ni and Ru cations to that determined for O3 was used to model P3 and O1 structures with partial Na occupations. We calculated E_c for $\frac{18!}{6!12!} = 18564$ structures to find the arrangement of 6 Na^{1+} in 18 Na sites for P3-$Na_6Ni_6Ru_3O_{18}$. For charge balancing, we considered Ni^{2+}/Ni^{3+} and Ru^{5+}. We performed DFT calculations on the electrostatically most favorable structure (with unequal distribution of Na ions in the three Na layers) and a structure (with equal distribution of Na ions in Na layers) whose energy was 0.16 eV (per formula unit) higher. We observed that the latter possessed the lowest total energy, and therefore, it was considered for further analysis. Finally, we calculated E_c for all possible configurations with various arrangements of 2 Na^{1+} in 12 Na sites as well as 6Ni^{3+} and 2Ni^{4+} in 8Ni sites, namely $\frac{12!}{2!10!} . \frac{8!}{6!2!} = 1848$, for O1-$Na_2Ni_8Ru_4O_{24}$. The structure with the lowest E_c value was considered for DFT calculation. The determined most favorable structure of each phase is presented in **Figure 6.**

Our lattice parameters computed using DFT calculation (**Table 1**) show that the Hubbard U correction is necessary to correctly compute both the a and c parameters of the O3-$Na[Ni_{2/3}Ru_{1/3}]O_2$ structure. By applying appropriate U values for Ni and Ru, we can also correctly predict the oxidation states of these cations. With the D3 dispersion correction, however, the c value calculated with PBE+U is underestimated. Both lattice parameters of P3-$Na_{2/3}[Ni_{2/3}Ru_{1/3}]O_2$ computed using the PBE+U method also agreed well with our XRD data. We observed that PBE+U+D3 underestimated the c value in the P3 structure as well; however, this parameter showed better agreement with our experiment for the O1-$Na_{1/6}[Ni_{2/3}Ru_{1/3}]O_2$ structure.

To study the electronic structures, we calculated the number of unpaired electrons (N_S↑− N_S↓), spin density difference (SDD), and density of states (DOS) using PBE+*U*+D3 (**Table 2**). It was observed that although the *U* correction significantly affected the electronic structure, including the D3 correction had almost no effect. Our calculations gave charge states of approximately 2+ (N_S↑− N_S↓=1.81) for all Ni cations and 5+ (N_S↑− N_S↓=3.03) for all Ru cations in the fully sodiated O3-$Na[Ni_{2/3}Ru_{1/3}]O_2$ structure. This can also be observed in the SDD plot, where large features exist on Ni and Ru. The small features on O indicate a small number of unpaired electrons, which is most likely due to the back donation of electrons from TMs to O in a real system compared with its perfect ionic crystal counterpart. Upon desodiation of x = 1.00 → 0.66 (O3-$Na[Ni_{2/3}Ru_{1/3}]O_2$ → P3-$Na_{2/3}[Ni_{2/3}Ru_{1/3}]O_2$), half of the Ni cations undergo oxidation from ~2+ to ~3+. This is evidenced by the small shrinkage of the SDD feature on half of the Ni cations (**Figure 7**) as well as the appearance of an up-spin peak at approximately 0.5 eV above the Fermi level (**Figure 8**). The desodiation-induced oxidation is not completely compensated by the oxidation of Ni. A fraction (2/3) of O anions is also slightly oxidized by approximately 0.08$|e|$, as concluded from the N_S↑− N_S↓ reduction from 0.08 to 0.00 for the O3 → P3 phase transition. This oxidation is also observed in SDD (**Figure 7**), for which the density features change their shapes, as well as in the DOS (**Figure 8**), where an extra up-spin p_O state appears at $E-E_F$ = ~0.5 eV in the DOS of the P3 structure compared with that of the O3 structure. The calculated N_S↑− N_S↓, SDD, and DOS data showed no significant changes for Ru. For the almost fully charged state, where the O1-$Na_{1/6}[Ni_{2/3}Ru_{1/3}]O_2$ structure is stabilized, 3/4 Ni possessed a charge state of ~3+, whereas the remaining 1/4 Ni had a charge state of ~4+. All of the O anions underwent slight oxidation, as clearly observed from the reduction in the magnetic moments of O anions, *i.e.*, more blue features in the SDD plots, and appearance of more depleted O states above the Fermi level (at $E-E_F$ = ~0.5 eV). This result confirms our experimental data (**Figure 4e and 4f**), indicating that O also participates in the redox reaction during charge/discharge. **Figure 8** demonstrates that in the O1 phase, there is a clear mixing of delocalized valence states of d_{Ni}, d_{Ru}, and p_{O}, particularly between −4 eV and −1 eV as well as hybridization between their localized states at $E-E_F$ = ~ −8.7 eV, indicating some covalent characteristics of the TM–O and TM–TM bonds in the charged system.

Operando differential electrochemical mass spectrometry (*o*-DEMS) measurement was conducted to validate the observed changes in oxygen that are solely associated with the oxygen redox (**Figure 9a**). Note that there was no evolution of O_2 or CO_2 gas moieties, indicating that the reversible O^{2-}/O^{1-} redox process dominates the activity of the $Na[Ni_{2/3}Ru_{1/3}]O_2$ electrode in the high-voltage region, O1 phase. From the above results, the Ni^{3+}/Ni^{2+} redox pair is predominant to $x = 0.67$ in $Na_{1-x}[Ni_{2/3}Ru_{1/3}]O_2$, during which multiple phase transitions progressed *via* O3–O'3–O"3–P3. The *a*-axis parameters gradually decrease in this range, and the tendency becomes steep in the range of the O"3–P3 phases. The oxidation of Ni^{2+} (0.69 Å) to Ni^{3+} (0.56 Å) is a possible reason for the reduction of the *a*-axis parameter. However, the expansion in the *c*-axis parameter is the result of the increased ionic character in the interlayers as Na^+ was extracted. As further Na^+ extraction progressed to $x = 0.79$ in $Na_{1-x}[Ni_{2/3}Ru_{1/3}]O_2$, the resulting *a*-axis is further contracted. Considering the inactivity of Ru^{5+}, the variation in the *a*-axis value is due to the oxidation of oxygen from O^{2-} (1.4 Å) to O^{1-} (1.32 Å), whereas the *c*-axis value remains almost constant. The volume variations were ΔV = ~2.9% for the O3–O1 phase transitions and ΔV = ~1.4% for the P3–O1 ones. Indeed, the mentioned plateaus, ~4 V on charge and ~3.5 V on discharge, correspond to the reaction mainly associated with oxygen redox. The series of reaction undergoes slow rather than the redox reaction by transition metal. For the reason, we measured Na^+ diffusivity for the initial two cycles using galvanostatic intermittent titration technique (GITT) in **Figure 9b**. GITT curves clearly demonstrate that the mentioned curve at high voltage did not disappear but become shortened due to the sluggish Na^+ diffusion at high voltage range (~10^{-11} – ~10^{-12} S cm^{-1}) for $Na_{1-x}[Ni_{2/3}Ru_{1/3}]O_2$ ($0.67 \leq x \leq 0.79$) *via* the O^{2-}/O^{1-} redox relative to the value below those plateaus (~10^{-9} – ~10^{-10} S cm^{-1}) for $Na_{1-x}[Ni_{2/3}Ru_{1/3}]O_2$ ($0 \leq x \leq 0.67$) *via* the Ni^{3+}/Ni^{2+} redox. Since Pauling electronegativity of Ru (2.2) is higher than other Ni (1.91) in $Na[Ni_{2/3}Ru_{1/3}]O_2$, the presenting covalence may impede the activity of lone pair electron in O 2*p* orbital.

The oxidation of O^{2-} to O^{1-} in $Na[Ni_{2/3}Ru_{1/3}]O_2$ electrode was confirmed by XANES measurements and proved with DFT calculations. DFT-SCAN calculations, which were applied to compute $N_S\uparrow - N_S\downarrow$, SDD, and DOS, revealed that the $Na[Ni_{2/3}Ru_{1/3}]O_2$ material experiences anionic redox during cycling. In addition, the obtained charge capacity in this work was approximately 165 mAh g^{-1}, which is consistent with ~0.79 mol Na^+ extraction from the formula unit. According to the XANES spectra for Ni (**Figure 4a**), Ni was oxidized from Ni^{2+} to Ni^{3+}. The reaction results in the capacity of approximately 140 mAh g^{-1}. From this consideration, the additional capacity of 25 mAh g^{-1} cannot be explained by the oxidation of Ni exceeding Ni^{3+}. Combining the theoretical investigation, *operando* XRD exhibiting a continuous decrease in the *a*-axis ascribed to the oxidation of oxygen that causes the reduction in ionic radius of oxygen in O1 phase range, and the GITT data, the oxidation of oxygen promotes the delivery of additional capacity 25 mAh g^{-1}, although the associated reaction was proceeded through the sluggish Na^+ diffusion at high voltage.

To understand the rapid capacity decay upon first cycles we analyze the surface of $Na[Ni_{2/3}Ru_{1/3}]O_2$ electrodes using time-of-flight secondary ion mass spectroscopy (ToF-SIMS) during first charge/discharge (**Figure S6**). For the fresh electrode $Na[Ni_{2/3}Ru_{1/3}]O_2$, fragments related to Na_2CO_3 as a NaC_2^+ ($m = 46.99$) and Na_2O as a Na_2O^+ ($m = 61.97$) were detected with small relative intensity. However, the intensity of these fragments gradually increased as the desodiation progressed to 3.2 V and, especially, to 4.1 V. This finding can be rooted to the growth the CEI resulting from copious electrolyte degradation at high voltage on the surface of electrode material. During discharge, decrease in the relative intensity was observed for the NaC_2^+ ($m = 46.99$) and Na_2O^+ ($m = 61.97$) fragments. Therefore, the capacity loss observed in $Na[Ni_{2/3}Ru_{1/3}]O_2$ material was mainly attributed to electrolyte degradation products, which lead to the formation of passivating layers that cause an increase in cell resistance, ultimate capacity loss and additional overvoltage.

Based on our findings, we can conclude that the Ni^{2+}/Ni^{3+} and O^{2-}/O^{1-} redox processes are responsible for the charge compensation mechanism in $Na[Ni_{2/3}Ru_{1/3}]O_2$, where the low plateaus are mainly governed by the cationic redox reaction and the higher plateau is mainly governed by the anionic oxygen redox reaction (**Figure 10a**). We compared the energy-density of O3-$Na[Ni_{2/3}Ru_{1/3}]O_2$ with those of reported oxygen-redox-assisted O3-compounds[38,40,41,50-55], including the very recent work by Tarascon et al.[56] (**Figure 10b and Table S3**). Apart from the high discharge capacity of about 190 mAh g^{-1} with an average operation voltage of 2.5 V (approximately 475 Wh $(kg\text{-}oxide)^{-1}$) for the O3 type $Na[Li_{1/3}Mn_{2/3}]O_2$, the evolution of O_2 gas associated with migration of Li toward Na layers during the first charge is the urgent issue to be resolved, because such oxygen residue is inclined to form sodium carbonates as a CEI layer and may arise safety concern when overcharged in real systems. Cao et al.[34] stabilized the oxygen redox chemistry in P2 $Na_{0.66}[Li_{0.22}Ru_{0.78}]O_2$; hence, the oxygen redox can be active in the non-bonding state of O 2*p*. Ru^{4+} was first oxidized to Ru^{5+}, and further desodiation led to oxidation of oxygen, resulting in additional capacity but no evolution of O_2 gas from the crystal structure. The series of reactions resulted in a discharge capacity of ~160 mAh g^{-1}. The presence of covalence character promoted by Ru in the structure suppressed the migration of Li to the Na layers, even though the oxygen redox was dominant in the Z-phase region, like the O2 or OP4 phase that provides octahedral coordinates for the highly desodiated state. The suppression of lithium migration and O_2 release enabled reversible electrochemical reaction for 500 cycles. The stoichiometric sodium Ru-based compounds O3-type $Na[Mg_{2/3}Ru_{1/3}]O_2$ and $Na[Mg_{1/2}Ru_{1/2}]O_2$ ($R\bar{3}m$) were electrochemically active achieved from oxygen-redox, as reported in the work of Zhou et al.[42]. Both materials were crystallized in the $R\bar{3}m$ space group; however, the oxidation state of Ru was different, namely Ru^{4+} in $Na[Mg_{1/2}Ru_{1/2}]O_2$ and Ru^{5+} in $Na[Mg_{2/3}Ru_{1/2}]O_2$, respectively. On the basis of *in situ* XRD, Raman, and DEMS analyses, it was shown that during the first charge, $Na[Mg_{2/3}Ru^{5+}_{1/3}]O_2$ underwent a simple O3–O'3 transition; however, a distorted structure was formed due to the O_2 release at the end of charge. A more complicated sequence of O3–O'3–P3 phase transitions was observed for $Na[Mg_{1/2}Ru^{4+}_{1/2}]O_2$, accompanied by sluggish kinetics without O_2 loss. They claimed that irreversible lattice oxygen loss in $Na[Mg_{2/3}Ru^{5+}_{1/3}]O_2$ and the formation of a distorted structure sacrificed for a more stable structure with solely Ru^{4+}/Ru^{5+} cationic redox for the subsequent cycling. The present O3-$Na[Ni_{2/3}Ru_{1/3}]O_2$ exhibits one of the highest energy densities and operation voltages demonstrating the importance of hybridization concept, combining redox activity of transition metal Ni^{3+}/Ni^{2+} with oxygen O^{2-}/O^{1-}, and no O_2 release during charging. The principal electrochemical problems in anion redox reactions in SIBs are the sluggish oxygen redox kinetics, high voltage hysteresis (compared to cationic redox), and voltage fade during cycling. The presence of electro-inactive Ru^{5+} in the O3-$Na[Ni_{2/3}Ru_{1/3}]O_2$ promotes such demerits for the oxygen redox reaction because the covalence provided by Ru^{5+}-O bond can suppress the cation disorder that transition metal migrates toward sodium layers during cycling, which in turn improves the electrochemical performance for prolonged cycles.

3. Conclusions

In this work, $Na[Ni_{2/3}Ru_{1/3}]O_2$ was investigated as a promising cathode material for SIBs. Combined electrochemical measurements, structural characterization, and first-principles DFT calculation revealed that the high capacity of 165 mAh g^{-1} for $Na[Ni_{2/3-x}Ru_{1/3}]O_2$ correlates strongly with cationic Ni^{3+}/Ni^{2+} and anionic O^{2-}/O^{1-} redox, suggesting a high tendency for reversibility. *Operando* XRD analysis revealed that $Na[Ni_{2/3}Ru_{1/3}]O_2$ undergoes multiple reversible phase changes in the sequence O3–O'3–O"3–P3–O1 in the voltage range of 2–4.1 V. The presence of Ru in the TM redox layer is effective for increasing the capacity and improving the structural stability. This work not only presents a highly efficient O3-type Ni-based sodium cathode but also provides a new path for the development of advanced cathodes *via* hybrid cationic and anionic redox processes.

4. Experimental

4.1. Synthesis

$Na[Ni_{2/3}Ru_{1/3}]O_2$ was synthesized via a solid-state method using Na_2CO_3 (Sigma Aldrich), NiO (Sigma Aldrich) and RuO_2 (ACROS Organics). A stoichiometric amount of each starting material with 5% excess of Na_2CO_3 was thoroughly mixed using a high-energy ball-mill at 380 rpm in ethanol for 6 h. The obtained powders were pelletized and calcined at 1050 °C for 10 h in O_2.

4.2. Material characterization

XRD was used to determine the crystal structure of $Na[Ni_{2/3}Ru_{1/3}]O_2$ using a PANalytical X'Pert diffractometer with a Cu Kα source in the angular range from 10° to 80° (2θ) at a step size of 0.03°, and the obtained data were refined using the Rietveld refinement program FULLPROF.[57] The as-synthesized materials were analyzed using ICP-AES (OPTIMA 8300, PerkinElmer). The morphology was investigated using SEM (Hitachi, SU-8010) and high-resolution TEM (Hitachi, H-800) coupled with EDX. Structural studies during cycling were performed using *operando* XRD (X'Pert, PANalytical diffractometer)[58-60] and *ex situ* XPS (K-Alpha, Thermo Scientific). *Ex situ* XANES measurement for the Ni K-edge and Ru K-edge region was performed in a transmission mode at beamline 8C at Pohang Accelerator Laboratory (PAL), South Korea. O K-edge XANES data were collected at beamline 2C of PAL using partial fluorescence yield (PFY) mode. To identify the surface states, we analyzed the O3-$Na[Ni_{2/3}Ru_{1/3}]O_2$ electrodes using time-of-flight secondary ion mass spectroscopy (ToF-SIMS; nanoTOF). *In situ* differential electrochemical mass spectrometry (DEMS) measurements were performed using a R2032 coin-type cell connected to a differential electrochemical mass spectrometry (DEMS) instrument (HPR-40 DEMS, Hiden Analytical). The mass spectrometer absolute sensitivity was calibrated for CO_2 and O_2 gases.

4.3. Electrochemical characterization

The electrodes were prepared by mixing 80 *wt*.% $Na[Ni_{2/3-x}Ru_{1/3}]O_2$ powder, 10 *wt*.% Super P, and 10 *wt*.% polyvinylidene fluoride (PVDF) binder in *N*-methyl-2-pyrrolidone (NMP). The obtained slurry mixture was applied on aluminum foil using a doctor blade followed by overnight drying at 120 °C in a vacuum oven. The R2032 coin-type cells were used for galvanostatic charge/discharge cycling. $NaNi_{2/3-x}Ru_{1/3}O_2$ electrodes were paired with Na metal separated by Whatman GF/C glass fiber in an electrolyte of 0.5 M $NaPF_6$ in propylene carbonate (PC) and fluoroethylene carbonate (FEC) (98:2 in volume). Assembly of the coin cells was performed in a Braun Ar-filled glove box with H_2O and O_2 contents of < 0.1 ppm. Galvanostatic charge and discharge measurements were conducted in the voltage range of 2–4.1 V at 25 °C for currents ranging from 0.05C to 20C (1C = 210 mA g^{-1}). GITT measurements were performed during 1-h charge and discharge with relaxation periods of 1 h at a current density of 0.05C (10.5 mA g^{-1}).

4.4. *Computation*

Spin-polarized DFT calculations were performed using the projector augmented wave (PAW)[61] potential method implemented in the Vienna *Ab Initio* Simulation Package (VASP).[62] The generalized gradient approximation (GGA) within the scheme of Perdew–Burke–Ernzerhof (PBE)[63] was used as the basis of the exchange-correlation (XC) functional. The Hubbard U correction proposed by Dudarev et al.[64] as well as the D3 dispersion correction of Grimme et al.[65] were also considered to find the best description to model the lattice parameters and electronic structures. The following $U-J$ (hereafter called U) values for Ni and Ru were tested: U(Ni)=6.8 eV and U(Ru)=3.0 eV, U(Ni)=6.8 eV and U(Ru)=8.0 eV. To perform the Coulomb energy analysis, we used a $(\sqrt{3}\times\sqrt{3})$R30 unit cell to model the O3-$NaNi_{2/3}Ru_{1/3}O_2$ ($Na_9Ni_6Ru_3O_{18}$) and P3-$Na_{2/3}Ni_{2/3}Ru_{1/3}O_2$ ($Na_6Ni_6Ru_3O_{18}$) structures and a

(2√3×2√3)R30 unit cell to model O1-$Na_{1/6}Ni_{2/3}Ru_{1/3}O_2$ ($Na_2Ni_4Ru_8O_{24}$). The DFT calculations were performed with the following unit cells: (2√3×2√3)R30 for O3, (√3×√3)R30 for P3, and (2√3×2√3)R30 for O1. To find the arrangement of Ni and Ru in the O3 structure, we had to use a [√3×√3] R30-type $Na_9Ni_6Ru_3O_{18}$ supercell to reduce the large number of possible combinations. For the DFT calculations, gamma-centered *k*-point meshes of 2×2×2, 3×3×1, and 2×2×4 were applied for the O3, P3, and O1 structures, respectively. We used an energy cutoff of 600 eV as well as electronic and force convergence criteria of 10^{-4} eV and 10^{-3} eV/Å, respectively. To construct the possible arrangements and compute their total Coulomb energies, we used the so-called *supercell* code.[66] The VESTA program[67] was applied to visualize the atomic structures.

Acknowledgements

This work was supported by the Basic Science Research Program through the National Research Foundation of Korea (NRF), funded by the Ministry of Education, Science, and Technology of Korea (NRF-2015M3D1A1069713, NRF-2019H1D8A2106002, NRF-2020R1A2B5B01095954, NRF-2020R1A6A1A03043435). The work was also supported by the Faculty Research Fund of Sejong University in 2021 (N. V. acknowledges support from Sejong University, “New Faculty Research Funds”). N. Y. and P. K. gratefully acknowledge support from the “Bundesministerium für Bildung und Forschung” (BMBF) as well as the computing time granted through JARA-HPC on the supercomputer JURECA at Forschungszentrum Jülich.

Appendix A. Supplementary data

Supplementary data to this article can be found online at

References

[1] B. Li, D. Xia, *Adv. Mater.* **2017**, *29*, 1.

[2] H. Xu, S. Guo, H. Zhou, *J. Mater. Chem. A* **2019**, *7*, 23662.

[3] G. Assat, J. M. Tarascon, *Nature Energy* **2018**, *3*, 373.

[4] A. Grimaud, W. T. Hong, Y. Shao-Horn, J. M. Tarascon, *Nat. Mater.* **2016**, *15*, 121.

[5] M. Li, T. Liu, X. Bi, Z. Chen, K. Amine, C. Zhong, J. Lu, *Chem. Soc. Rev.* **2020**, *49*, 1688.

[6] C. Li, F. Geng, B. Hu, *Mater. Today Energy* **2020**, *17*, 100474.

[7] J. Rouxel, *Angew. Chem. Inter. Ed.* **1996**, *35*, 1053.

[8] S. Saha, G. Assat, M. T. Sougrati, D. Foix, H. Li, J. Vergnet, S. Turi, Y. Ha, W. Yang, J. Cabana, G. Rousse, A. M. Abakumov, J. M. Tarascon, *Nature Energy* **2019**, *4*, 977.

[9] N. Voronina, H. Yashiro, S. T. Myung, *J. Mater. Chem. A* **2018**, *6*, 17111.

[10] J. Hong, W. E. Gent, P. Xiao, K. Lim, D. H. Seo, J. Wu, P. M. Csernica, C. J. Takacs, D. Nordlund, C. J. Sun, K. H. Stone, D. Passarello, W. Yang, D. Prendergast, G. Ceder, M. F. Toney, W. C. Chueh, *Nat. Mater.* **2019**, *18*, 256.

[11] T. Ohzuku, M. Nagayama, K. Tsuji, K. Ariyoshi, *J. Mater. Chem.* **2011**, *21*, 10179.

[12] K. Luo, M. R. Roberts, R. Hao, N. Guerrini, D. M. Pickup, Y. S. Liu, K. Edström, J. Guo, A. V. Chadwick, L. C. Duda, P. G. Bruce, *Nat. Chem.* **2016**, *8*, 684.

[13] H. Yu, R. Ishikawa, Y. G. So, N. Shibata, T. Kudo, H. Zhou, Y. Ikuhara, *Angew. Chem. Inter. Ed.* **2013**, *52*, 5969.

[14] J. Zheng, S. Myeong, W. Cho, P. Yan, J. Xiao, C. Wang, J. Cho, J. G. Zhang, *Adv. Energy Mater.* **2017**, 22, 1601284.

[15] B. Li, R. Shao, H. Yan, L. An, B. Zhang, H. Wei, J. Ma, D. Xia, X. Han, *Adv. Funct. Mater.* **2016**, *26*, 1330.

[16] P. E. Pearce, A. J. Perez, G. Rousse, M. Saubanère, D. Batuk, D. Foix, E. McCalla, A. M. Abakumov, G. Van Tendeloo, M. L. Doublet, J. M. Tarascon, *Nat. Mater.* **2017**,

16, 580.

[17] E. Boivin, N. Guerrini, R. A. House, J. G. Lozano, L. Jin, G. J. Rees, J. W. Somerville, C. Kuss, M. R. Roberts, P. G. Bruce, *Adv. Funct. Mater.* **2021**, *31*, 2003660.

[18] F. Wu, G. T. Kim, M. Kuenzel, H. Zhang, J. Asenbauer, D. Geiger, U. Kaiser, S. Passerini, *Adv. Energy Mater.* **2019**, *9*, 1902445.

[19] M. Sathiya, G. Rousse, K. Ramesha, C. P. Laisa, H. Vezin, M. T. Sougrati, M. L. Doublet, D. Foix, D. Gonbeau, W. Walker, A. S. Prakash, M. Ben Hassine, L. Dupont, J. M. Tarascon, *Nat. Mater.* **2013**, *12*, 827.

[20] M. Sathiya, A. M. Abakumov, D. Foix, G. Rousse, K. Ramesha, M. Saubanère, M. L. Doublet, H. Vezin, C. P. Laisa, A. S. Prakash, D. Gonbeau, G. Vantendeloo, J. M. Tarascon, *Nat. Mater.* **2015**, *14*, 230.

[21] N. Voronina, Y. K. Sun, S. T. Myung, *ACS Energy Lett.* **2020**, *5*, 1814.

[22] L. Li, F. C. Castro, J. S. Park, H. Li, E. Lee, T. D. Boyko, J. W. Freeland, Z. Yao, T. T. Fister, J. Vinson, E. L. Shirley, C. Wolverton, J. Cabana, V. P. Dravid, M. M. Thackeray, M. K. Y. Chan, *Chem. Mater.* **2019**, *31*, 4341.

[23] A. Konarov, J. H. Jo, J. U. Choi, Z. Bakenov, H. Yashiro, J. Kim, S. T. Myung, *Nano Energy* 2019, *59*, 197.

[24] A. Konarov, H. J. Kim, J. H. Jo, N. Voronina, Y. Lee, Z. Bakenov, J. Kim, S. T. Myung, *Adv.Energy Mater.* **2020**, *10*, 2001111.

[25] H. J. Kim, A. Konarov, J. H. Jo, J. U. Choi, K. Ihm, H. K. Lee, J. Kim, S. T. Myung, *Adv. Energy Mater.* **2019**, *9*, 1901181.

[26] X. Rong, J. Liu, E. Hu, Y. Liu, Y. Wang, J. Wu, X. Yu, K. Page, Y. S. Hu, W. Yang, H. Li, X. Q. Yang, L. Chen, X. Huang, *Joule* **2018**, *2*, 125.

[27] B. Song, E. Hu, J. Liu, Y. Zhang, X. Q. Yang, J. Nanda, A. Huq, K. Page, *J. Mater. Chem. A* **2019**, *7*, 1491.

[28] N. Yabuuchi, R. Hara, K. Kubota, J. Paulsen, S. Kumakura, S. Komaba, *J. Mater.*

Chem. A **2014**, *2*, 16851.

[29] X. Bai, M. Sathiya, B. Mendoza-Sánchez, A. Iadecola, J. Vergnet, R. Dedryvère, M. Saubanère, A. M. Abakumov, P. Rozier, J. M. Tarascon, *Advanced Energy Materials* **2018**, *8*, 1802379.

[30] E. De La Llave, E. Talaie, E. Levi, P. K. Nayak, M. Dixit, P. T. Rao, P. Hartmann, F. Chesneau, D. T. Major, M. Greenstein, D. Aurbach, L. F. Nazar, *Chem. Mater.* **2016**, *28*, 9064.

[31] R. A. House, U. Maitra, L. Jin, J. G. Lozano, J. W. Somerville, N. H. Rees, A. J. Naylor, L. C. Duda, F. Massel, A. V. Chadwick, S. Ramos, D. M. Pickup, D. E. McNally, X. Lu, T. Schmitt, M. R. Roberts, P. G. Bruce, *Chem. Mater.* **2019**, *31*, 3293.

[32] P. F. Wang, Y. Xiao, N. Piao, Q. C. Wang, X. Ji, T. Jin, Y. J. Guo, S. Liu, T. Deng, C. Cui, L. Chen, Y. G. Guo, X. Q. Yang, C. Wang, *Nano Energy* **2020**, *69*, 104474.

[33] Y. Xiao, Y. F. Zhu, H. R. Yao, P. F. Wang, X. D. Zhang, H. Li, X. Yang, L. Gu, Y. C. Li, T. Wang, Y. X. Yin, X. D. Guo, B. H. Zhong, Y. G. Guo, *Adv. Energy Mater.* **2019**, *9*, 1803978.

[34] X. Cao, H. Li, Y. Qiao, X. Li, M. Jia, J. Cabana, H. Zhou, *Adv. Energy Mater.* **2020**, *10*, 1903785.

[35] A. Konarov, H. J. Kim, N. Voronina, Z. Bakenov, S. T. Myung, *ACS Appl. Mater. Interfaces* **2019**, *11*, 28928.

[36] K. Dai, J. Mao, Z. Zhuo, Y. Feng, W. Mao, G. Ai, F. Pan, Y. de Chuang, G. Liu, W. Yang, *Nano Energy* **2020**, 74, 104831.

[37] W. Zheng, Q. Liu, Z. Wang, Z. Wu, S. Gu, L. Cao, K. Zhang, J. Fransaer, Z. Lu, Energy Storage Mater. **2020**, *28*, 300.

[38] M. Tamaru, X. Wang, M. Okubo, A. Yamada, *Electrochem. Commun.* **2013**, *33*, 23.

[39] B. Mortemard De Boisse, G. Liu, J. Ma, S. I. Nishimura, S. C. Chung, H. Kiuchi, Y. Harada, J. Kikkawa, Y. Kobayashi, M. Okubo, A. Yamada, *Nat. Commun.* **2016**, *7*,

11397.

[40] P. Rozier, M. Sathiya, A.-R. Paulraj, D. Foix, T. Desaunay, P.-L. Taberna, P. Simon, J.-M. Tarascon, *Electrochem. Commun.* **2015**, *53*, 29.

[41] A. J. Perez, D. Batuk, M. Saubanère, G. Rousse, D. Foix, E. McCalla, E. J. Berg, R. Dugas, K. H. W. Van Den Bos, M. L. Doublet, D. Gonbeau, A. M. Abakumov, G. Van Tendeloo, J. M. Tarascon, *Chem. Mater.* **2016**, *28*, 8278.

[42] M. Jia, Y. Qiao, X. Li, K. Jiang and H. Zhou, *J. Mater. Chem. A*, **2019**, *7*, 20405.

[43] Q. Li, S. Xu, S. Guo, K. Jiang, X. Li, M. Jia, P. Wang, H. Zhou, *Adv. Mater.* **2020**, *32*, 1907936.

[44] G. Assat, A. Iadecola, C. Delacourt, R. Dedryvère, J. M. Tarascon, *Chem. Mater.* **2017**, *29*, 9714.

[45] H. Li, S. Ramakrishnan, J. W. Freeland, B. D. McCloskey, J. Cabana, *J. Am. Chem. Soc.* **2020**, *142*, 8160.

[46] Q. Wang, K. Jiang, Y. Feng, S. Chu, X. Zhang, P. Wang, S. Guo, H. Zhou, *ACS Appl. Mater. Interfaces* **2020**, *12*, 39056.

[47] Y. Qiao, S. Guo, K. Zhu, P. Liu, X. Li, K. Jiang, C. J. Sun, M. Chen, H. Zhou, *Energy Environ. Sci.* **2018**, *11*, 299.

[48] S. Song, M. Kotobuki, F. Zheng, Q. Li, C. Xu, Y. Wang, W. D. Z. Li, N. Hu, L. Lu, *J. Power Sources* **2017**, *342*, 685.

[49] K. Xi, S. Chu, X. Zhang, X. Zhang, H. Zhang, H. Xu, J. Bian, T. Fang, S. Guo, P. Liu, M. Chen, H. Zhou, *Nano Energy* **2020**, *67*, 104215.

[50] M. Jia, Y. Qiao, X. Li, F. Qiu, X. Cao, P. He, H. Zhou, *ACS Appl. Mater. Interfaces* **2020**, *12*, 851.

[51] X. Zhang, Y. Qiao, S. Guo, K. Jiang, S. Xu, H. Xu, P. Wang, P. He, H. Zhou, *Adv. Mater.* **2019**, *31*, 1807770.

[52] C. Zhao, Q. Wang, Y. Lu, B. Li, L. Chen, Y. S. Hu, *Sci. Bul.* **2018**, *63*, 1125.

[53] T. Zhu, P. Hu, C. Cai, Z. Liu, G. Hu, Q. Kuang, L. Mai, L. Zhou, *Nano Energy* **2020**, *70*, 104548.

[54] T. Zhu, P. Hu, X. Wang, Z. Liu, W. Luo, K. A. Owusu, W. Cao, C. Shi, J. Li, L. Zhou, L. Mai, *Adv. Energy Mater.* **2019**, *9*, 1803436.

[55] X. Li, S. Guo, F. Qiu, L. Wang, M. Ishida, H. Zhou, *J. Mater. Chem. A*, **2019**, *7*, 4396.

[56] Q. Wang, S. Mariyappan, G. Rousse, A. V. Morozov, B. Porcheron, R. Dedryvère, J. Wu, W. Yang, L. Zhang, M. Chakir, M. Avdeev, M. Deschamps, Y. S. Yu, J. Cabana, M. L. Doublet, A. M. Abakumov, J. M. Tarascon, *Nat. Mater.* **2021**, *20*, 353.

[57] J. Rodríguez-Carvajal, *Physica B: Physics of Condensed Matter* **1993**, *192*, 55.

[58] N. Voronina, J. H. Jo, J. U. Choi, A. Konarov, J. Kim, S. T. Myung, *J. Power Sources* **2020**, *455*, 227976.

[59] J. U. Choi, C. S. Yoon, Q. Zhang, P. Kaghazchi, Y. H. Jung, K. S. Lee, D. C. Ahn, Y. K. Sun, S. T. Myung, *J. Mater. Chem. A* **2019**, *7*, 202.

[60] J. U. Choi, Y. J. Park, J. H. Jo, L. Y. Kuo, P. Kaghazchi, S. T. Myung, *ACS Appl. Mater. Interfaces* **2018**, *10*, 40978.

[61] P. E. Blöchl, *Phys. Rev. B* **1994**, *50*, 17953.

[62] G. Kresse, J. Furthmüller, *Comput. Mater. Sci.* **1996**, *6*, 15.

[63] J. P. Perdew, K. Burke and M. Ernzerhof, *Phys. Rev. Lett.*, **1997**, *78*, 1396.

[64] S. L. Dudarev, G. A. Botton, S. Y. Savrasov, C. J. Humphreys, and A. P. Sutton. *Phys. Rev. B*, **1998**, *57*, 1505.

[65] S. Grimme, *J. Comput. Chem.* **2006**, *27*, 1787.

[66] K. Okhotnikov, T. Charpentier, S. Cadars, *J. Cheminformatics* **2016**, *8*, 1.

[67] K. Momma, F. Izumi, *J. Appl. Crystallogr.* **2011**, *44*, 1272.

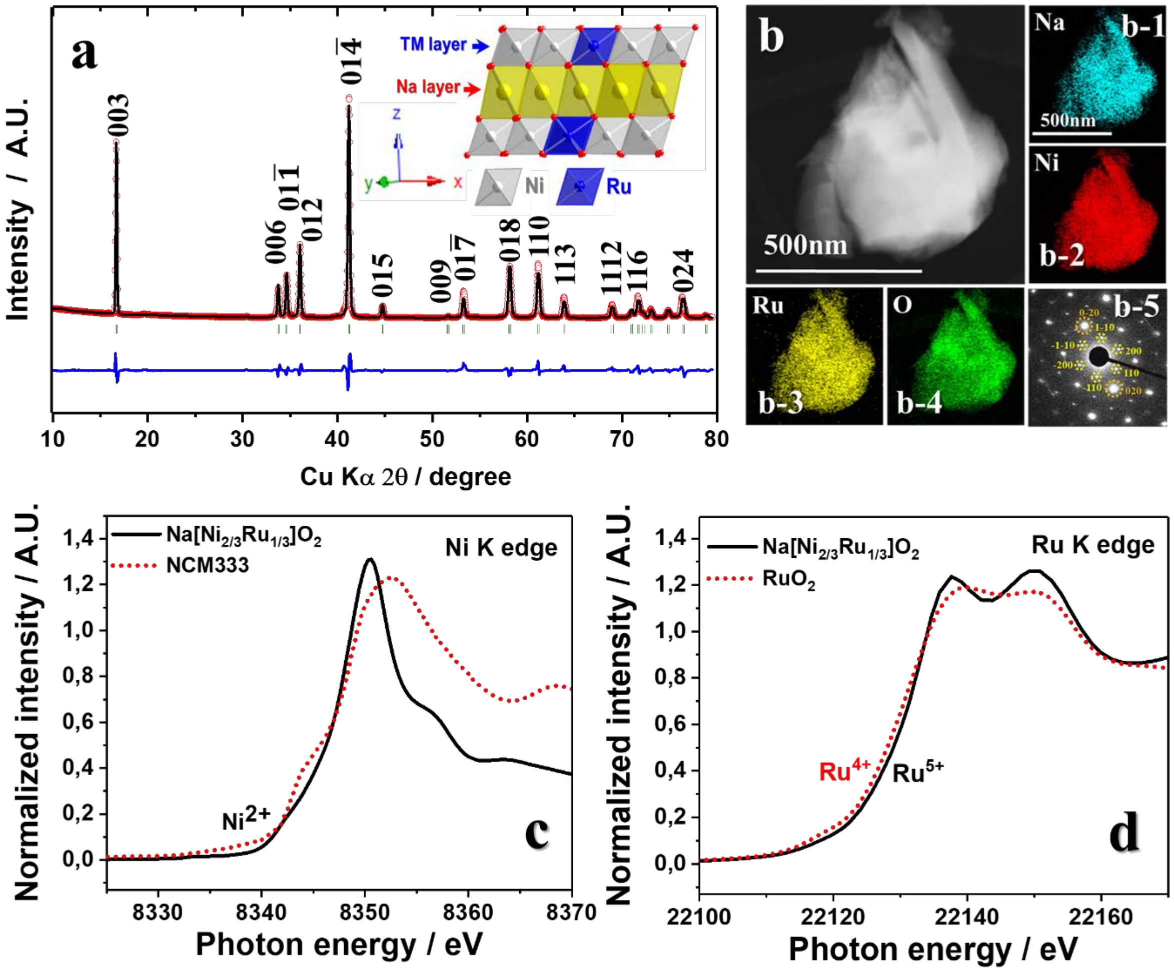

Figure 1. (a) Rietveld refinement results of XRD data and the corresponding crystal structure for Na[$Ni_{2/3}Ru_{1/3}$]O_2; (b) TEM image of Na[$Ni_{2/3}Ru_{1/3}$]O_2 and the corresponding EDX mappings of (b-1) Na, (b-2) Ni, (b-3) Ru, and (b-4) O and (b-5) selected-area electron diffraction pattern along the [001] zone axis; (c) Ni K-edge and (d) Ru K-edge XANES spectra of Na[$Ni_{2/3}Ru_{1/3}$]O_2.

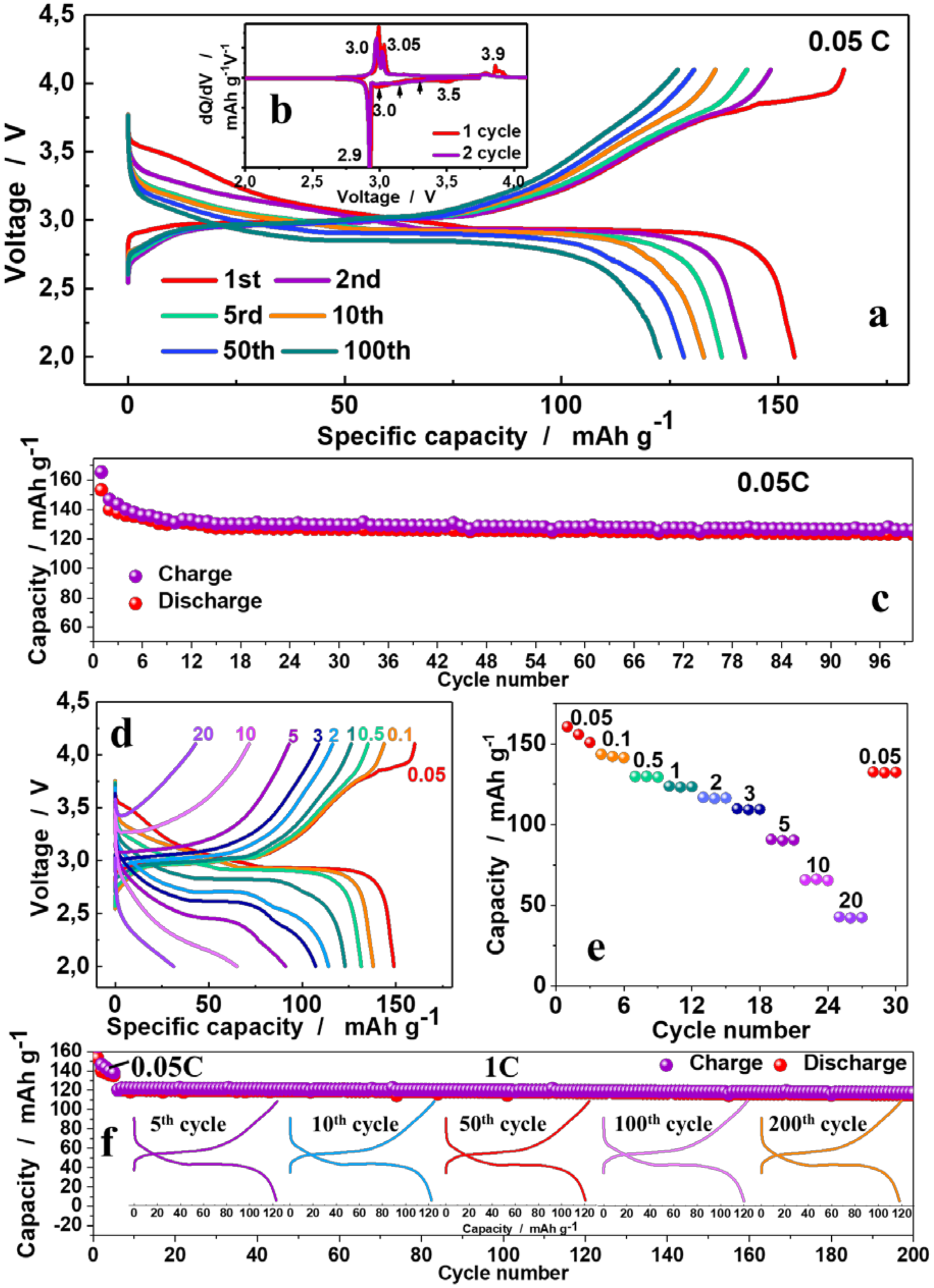

Figure 2. (a) Voltage profiles of Na[$Ni_{2/3}Ru_{1/3}$]O_2 tested in the voltage range of 2–4.1 V at 10.5 mA g^{-1}, (b) differential capacity plot of Na[$Ni_{2/3}Ru_{1/3}$]O_2, (c) cycling performance of

$Na[Ni_{2/3}Ru_{1/3}]O_2$ at 0.05C, (d) voltage profiles and (e) rate capability from 0.05C to 20C of $Na[Ni_{2/3}Ru_{1/3}]O_2$, and (f) and cycling performance of $Na[Ni_{2/3}Ru_{1/3}]O_2$ at 1C.

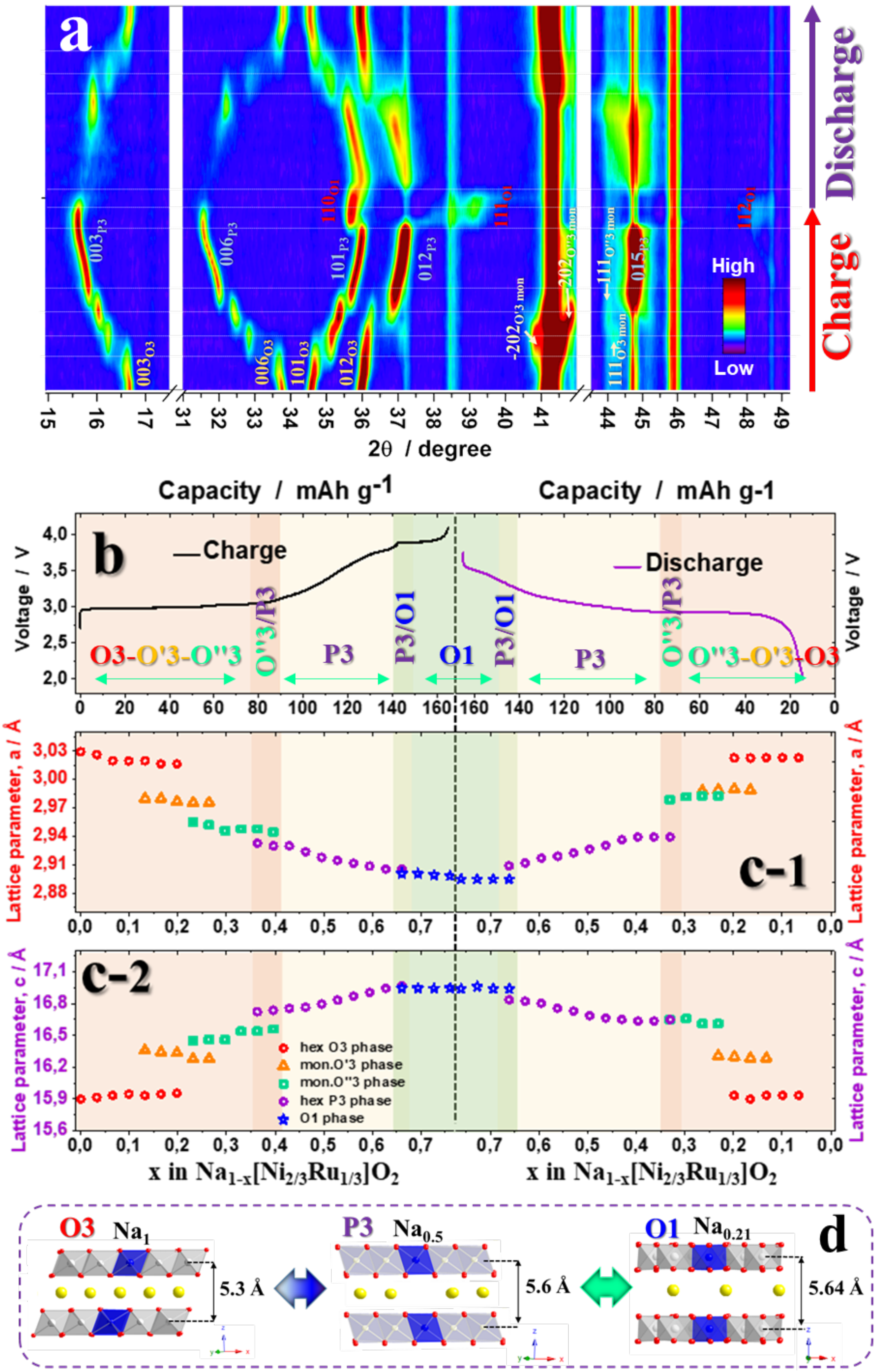

Figure 3. Structural evolution of $Na[Ni_{2/3}Ru_{1/3}]O_2$: (a) 2D image of *operando* XRD data during the first charge/discharge; (b) voltage profile of $Na[Ni_{2/3}Ru_{1/3}]O_2$ during first charge and

discharge; corresponding (c-1) *a*-axis and (c-2) *c*-axis lattice parameters calculated from *operando* XRD results; (d) schematic illustration of structure for O3, P3, and O1 plotted based on the results in (c).

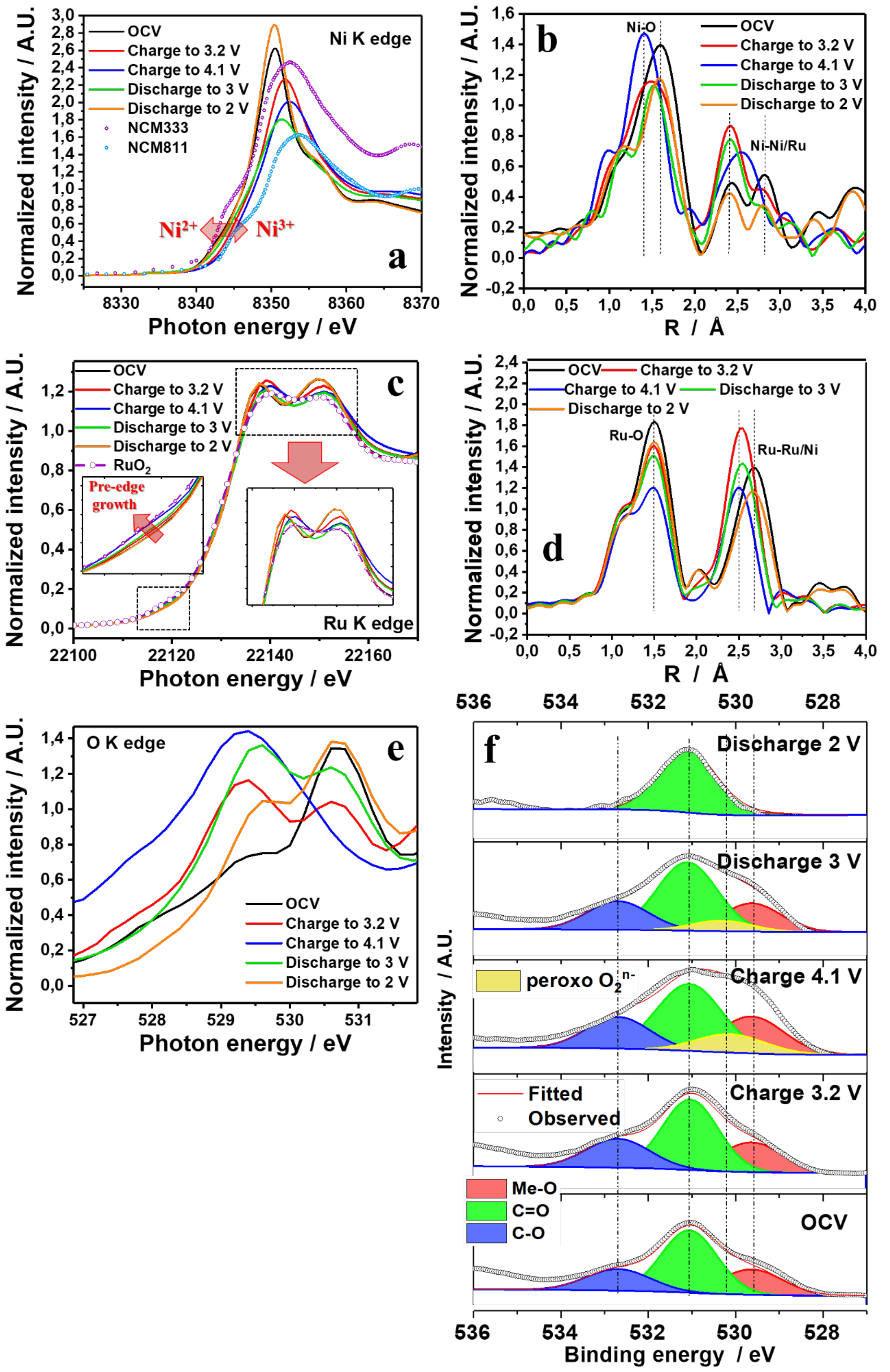

Figure 4. XANES, EXAFS, and XPS spectra measured at OCV, half charge (3.2 V), full charge (4.1 V), half discharge (3 V), and full discharge (2 V) for $Na[Ni_{2/3}Ru_{1/3}]O_2$ electrode: (a) Ni K-

edge XANES spectrum, (b) Ni K-edge EXAFS spectrum, (c) Ru K-edge XANES spectrum, (d) Ru K-edge EXAFS spectrum, (e) O K-edge XANES spectrum, and (f) XPS spectrum of O1*s*.

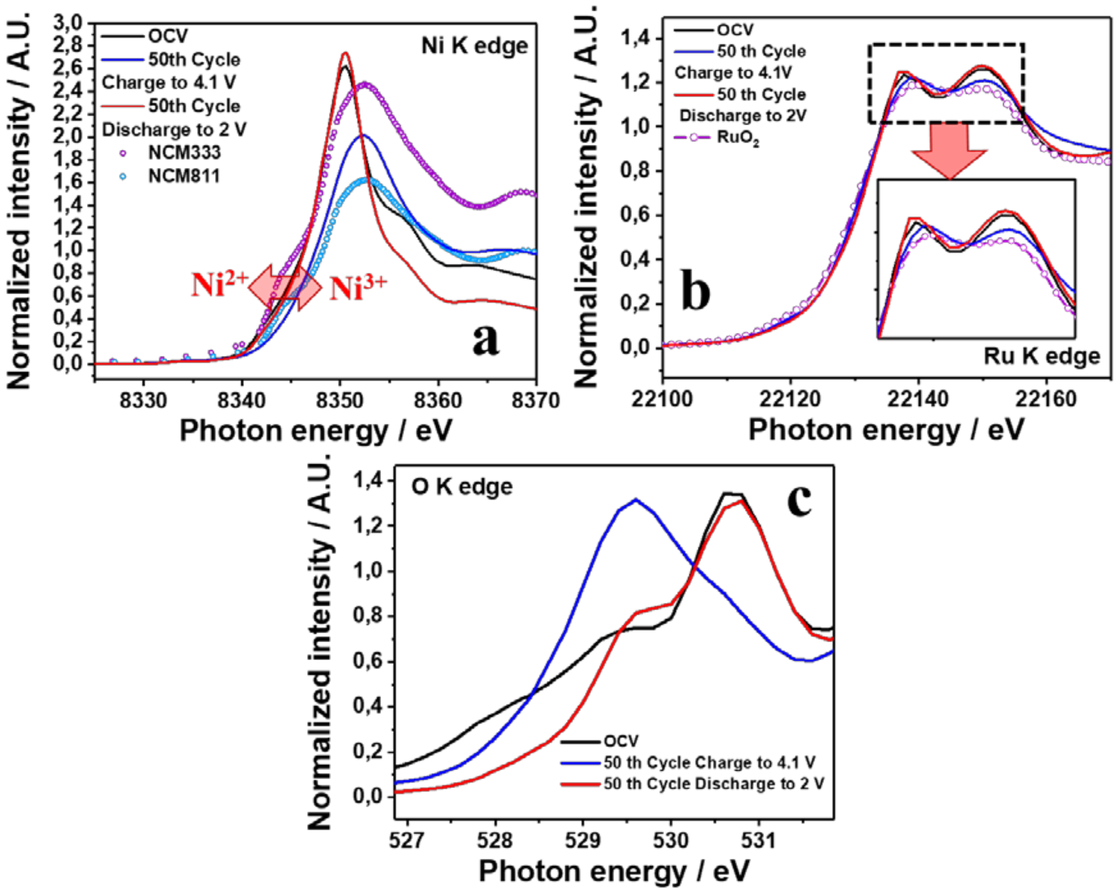

Figure 5. XANES spectra measured at OCV, 50th full charge (4.1 V), and 50th full discharge (2 V) for $Na[Ni_{2/3}Ru_{1/3}]O_2$ electrode: (a) Ni K-edge, (b) Ru K-edge, and (c) O K-edge.

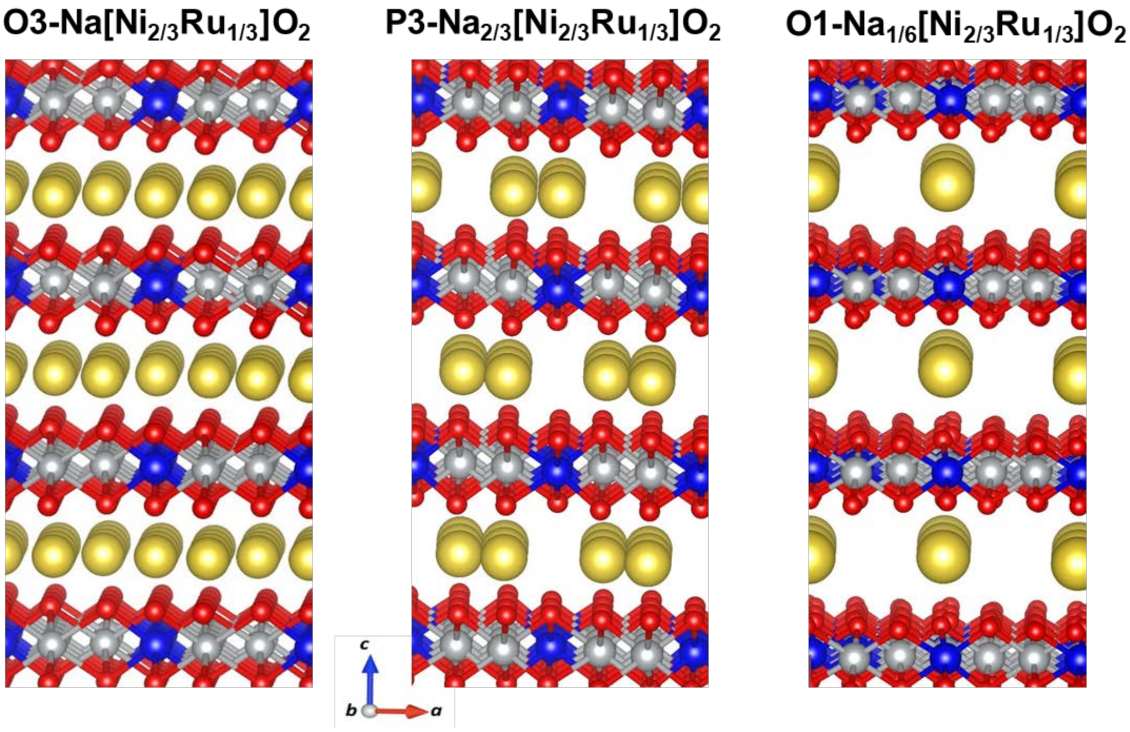

Figure 6. Calculated atomic structures of $Na_x[Ni_{2/3}Ru_{1/3}]O_2$. The yellow, red, grey, and blue colors represent Na, O, Ni, and Ru ions, respectively.

Table 1. Calculated lattice parameters for the O3, P3, and O1 phases representing $Na_x[Ni_{2/3}Ru_{1/3}]O_2$ structures from the fully discharged to nearly fully charged states using DFT with PBE exchange-correlation (XC) functional as well as PBE+Hubbard *U* without and with dispersion D3 corrections.

System	**PBE**		**PBE+*U*** ***U*(Ni)=6.8 eV** ***U*(Ru)=8.0 eV**		**PBE+*U*+D3** ***U*(Ni)=6.8 eV** ***U*(Ru)=8.0 eV**	
	a [Å]	*c* [Å]	*a* [Å]	*c* [Å]	*a* [Å]	*c* [Å]
O3-$Na[Ni_{2/3}Ru_{1/3}]O_2$	3.06	15.67	3.03	15.89	3.00	15.67
P3-$Na_{2/3}[Ni_{2/3}Ru_{1/3}]O_2$	2.92	16.35	2.93	16.59	2.90	16.35
O1-$Na_{1/6}[Ni_{2/3}Ru_{1/3}]O_2$	2.93	5.92	2.91	6.03	2.89	5.86

Table 2. Calculated average number of unpaired electrons in O3-Na[$Ni_{2/3}Ru_{1/3}$]O_2, P3-$Na_{0.33}$[$Ni_{2/3}Ru_{1/3}$]O_2, P3-$Na_{0.66}$[$Ni_{2/3}Ru_{1/3}$]O_2, and O1-$Na_{0.166}$[$Ni_{2/3}Ru_{1/3}$]O_2 with PBE+*U*+D3: *U*(Ni)=6.8 eV, *U*(Ru)=8.0 eV.

System	Na	Ni	Ru	O
O3-Na[$Ni_{2/3}Ru_{1/3}$]O_2	0.00	1.90	3.03	0.08
P3-$Na_{2/3}$[$Ni_{2/3}Ru_{1/3}$]O_2	0.00	$Ni_{1/3}$ = 1.80 $Ni_{1/3}$ = 1.24	3.02	$O_{2/3}$ = -0.0 $O'_{1/3}$ = 0.10
O1-$Na_{1/6}$[$Ni_{2/3}Ru_{1/3}$]O_2	0.00	$Ni_{1/2}$ = 1.26 $Ni_{1/6}$ = 0.12	3.00	$O_{1/2}$ = -0.03 $O'_{1/4}$ = -0.10 $O''_{1/4}$ = 0.06

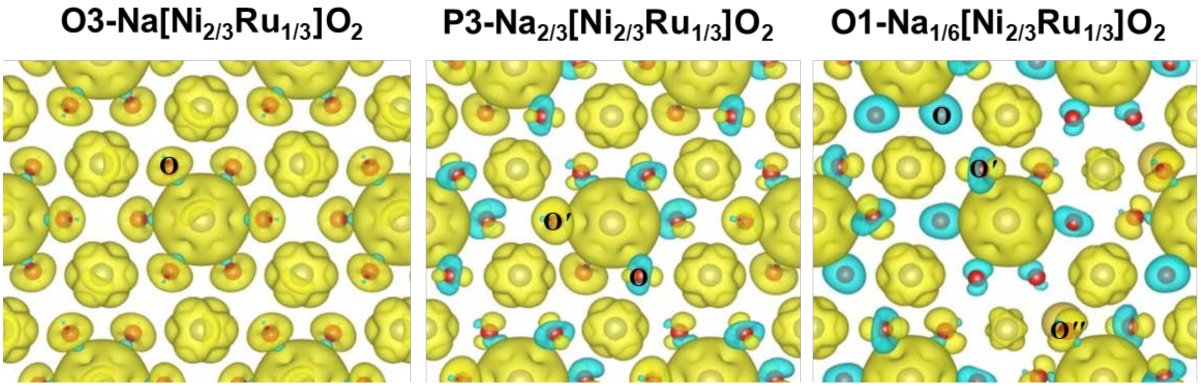

O3-$Na[Ni_{2/3}Ru_{1/3}]O_2$ P3-$Na_{2/3}[Ni_{2/3}Ru_{1/3}]O_2$ O1-$Na_{1/6}[Ni_{2/3}Ru_{1/3}]O_2$

Figure 7. Calculated spin density differences (isosurface of 0.008 eV/Å^3) in $Na_x[Ni_{2/3}Ru_{1/3}]O_2$ structures using PBE+U+D3: U(Ni)=6.8 eV, U(Ru)=8.0 eV. The up- and down-spin electrons are in yellow and blue, respectively.

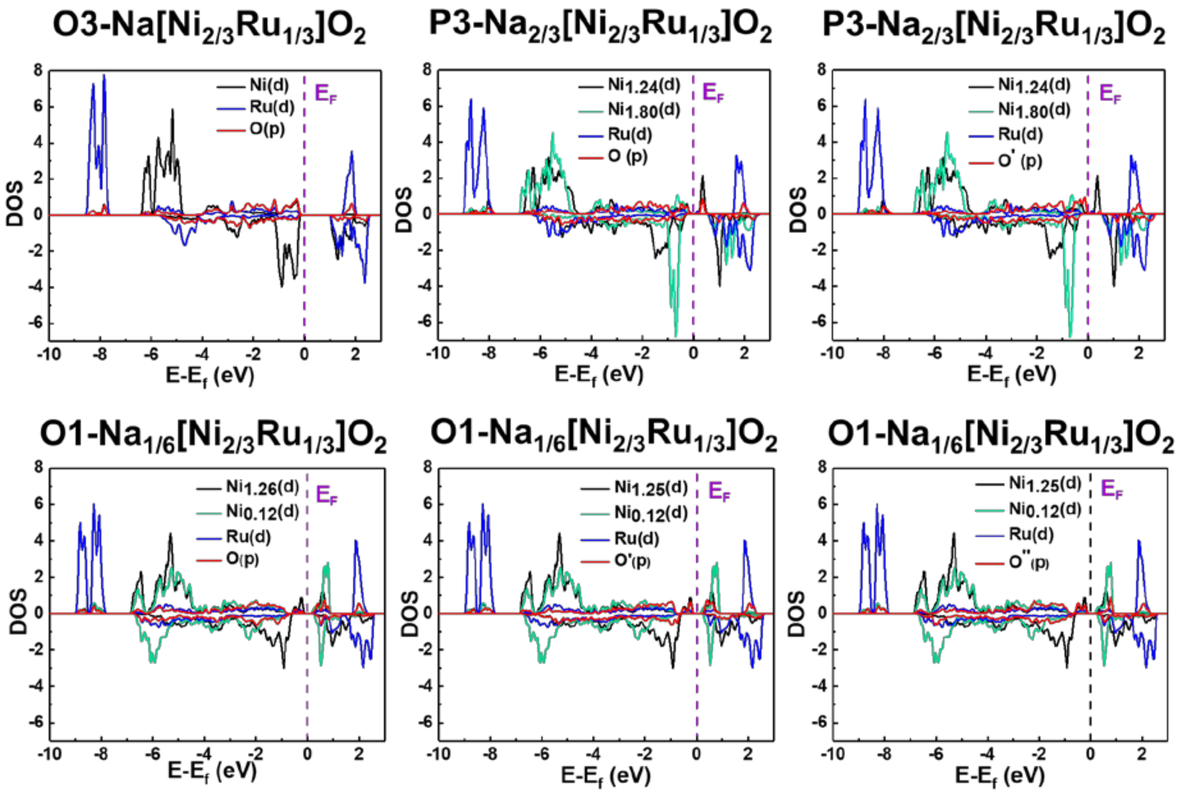

Figure 8. Partial density of states (PDOS) of $Na_x[Ni_{2/3}Ru_{1/3}]O_2$ structures. For P3 and O3, the PDOSs are plotted separately for various types of O anions as characterized by their $N_{S\uparrow} - N_{S\downarrow}$ (see **Table 2**): O, O′ and O″ (see **Figure 7**). The Fermi level was set to zero.

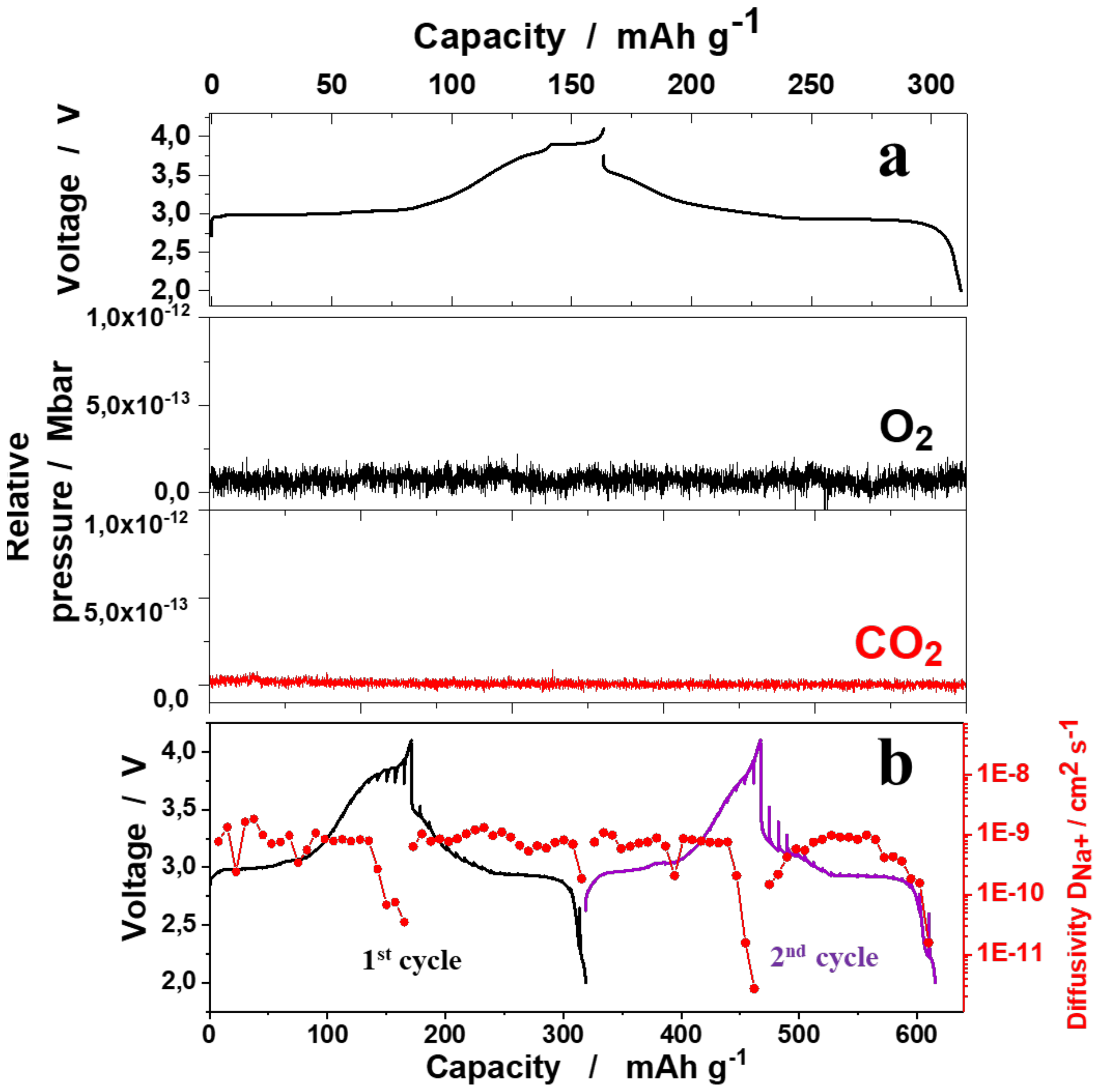

Figure 9. (a) *Operando* DEMS results of gas evolution for O_2 and CO_2 in $Na[Ni_{2/3}Ru_{1/3}]O_2$ at 0.1C. (b) GITT curve of 1st and 2nd cycles and the corresponding calculated Na^+ diffusion coefficients.

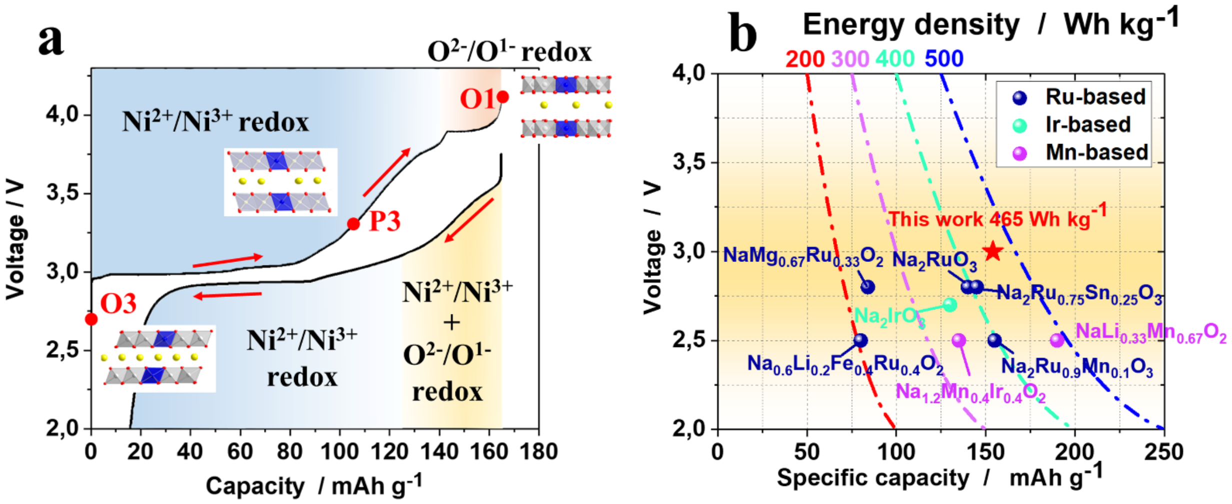

Figure 10. (a) Schematic illustration of the reaction mechanism of the $Na[Ni_{2/3}Ru_{1/3}]O_2$. (b) Comparison of performance of reported oxygen-redox-based O3-type cathode materials for SIBs.

We investigate O3-type layered $Na[Ni_{2/3}Ru_{1/3}]O_2$ cathode material with both cationic and anionic redox highlighted by theoretical and mechanistic properties. Ru provides partial covalent bonding in the charged system, with acceptable structural and cycling stability accompanied by Ni^{2+}/Ni^{3+} and O^{2-}/O^{1-} redox pairs without O_2 gas loss in Na cells.

Keywords: Cathode; Cationic; Anionic; Redox; Sodium; Battery.

N.Voronina, N. Yaqoob, H. J. Kim, K.-S. Lee, H.-D. Lim, H.-G. Jung, O. Guillon, P. Kaghazchi*, S.-T. Myung*

A New Approach to Stable Cationic and Anionic Redox Activity in O3-Layered Cathode for Sodium-Ion Batteries

TOC

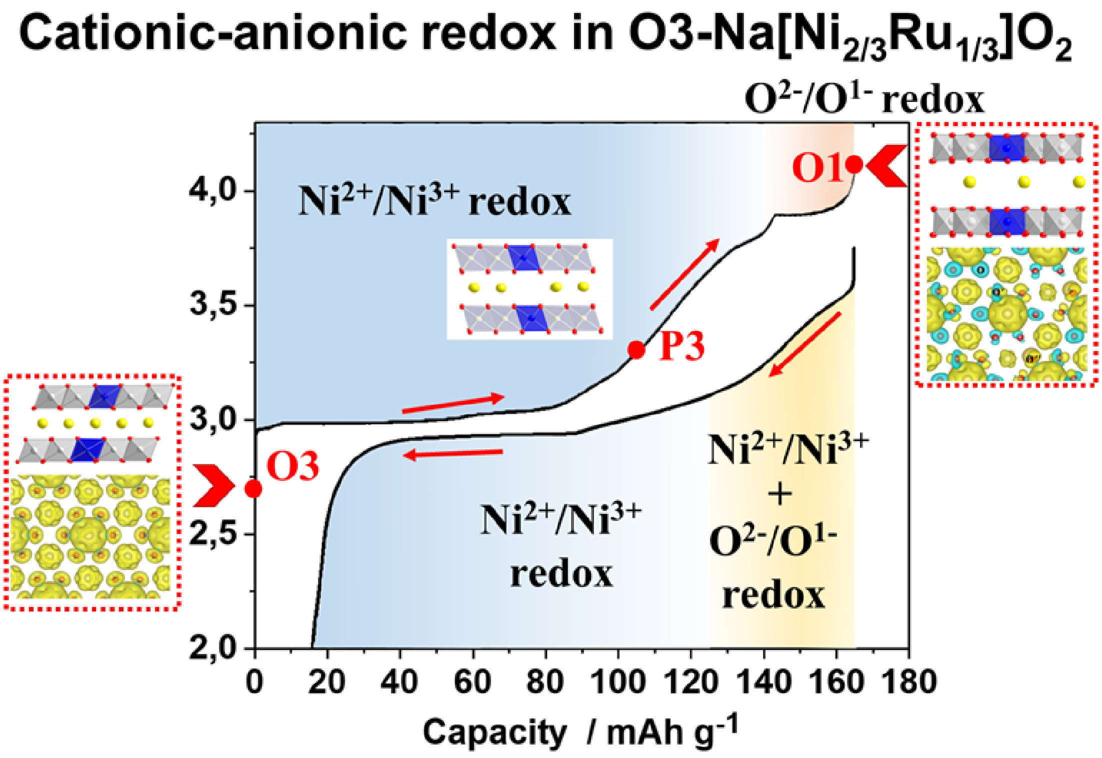

Supporting Information

A New Approach to Stable Cationic and Anionic Redox Activity in O3-Layered Cathode for Sodium-Ion Batteries

Natalia Voronina,[a] Najma Yaqoob,[b] Hee Jae Kim,[a] Kug-Seung Lee,[c] Hee-Dae Lim,[d] Hun-Gi Jung,[d] Olivier Guillon,[b] Payam Kaghazchi,[b,]* *Seung-Taek Myung*[a,]*

[a]*Hybrid Materials Research Center, Department of Nano Technology and Advanced Materials Engineering, Sejong Battery Institute, Sejong University, Seoul, 05006, South Korea*

[b]*Forschungszentrum Jülich GmbH, Institute of Energy and Climate Research, Materials Synthesis and Processing (IEK-1), Jülich, Germany*

[c]*Pohang Accelerator Laboratory, 80 Jigokro-127-beongil, Nam-gu, Pohang, Gyeongbuk 37673, South Korea*

[d]*Center for Energy Storage Research, Korea Institute of Science and Technology, Seoul, 02792, South Korea*

E-mail: p.kaghazchi@fz-juelich.de (P. Kaghazchi)
E-mail: smyung@sejong.ac.kr (S. Myung)

Table S1. Rietveld refinement results of the XRD data for $Na[Ni_{2/3}Ru_{1/3}]O_2$.

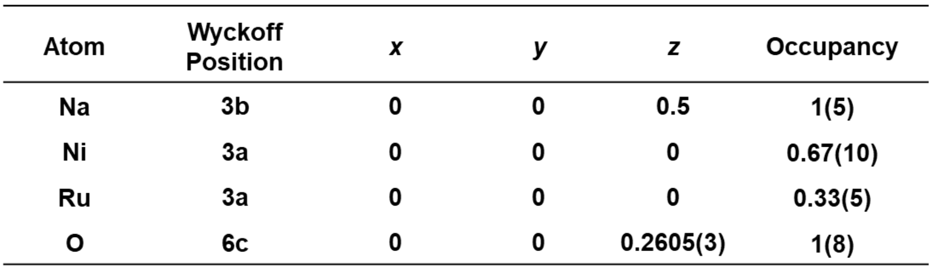

Atom	Wyckoff Position	*x*	*y*	*z*	Occupancy
Na	3b	0	0	0.5	1(5)
Ni	3a	0	0	0	0.67(10)
Ru	3a	0	0	0	0.33(5)
O	6c	0	0	0.2605(3)	1(8)

O3 - Space group $R\overline{3}m$ a : 3.0310(9) Å, c : 15.9353(9) Å; Rp: 9.21 %, Rwp: 12.7 %

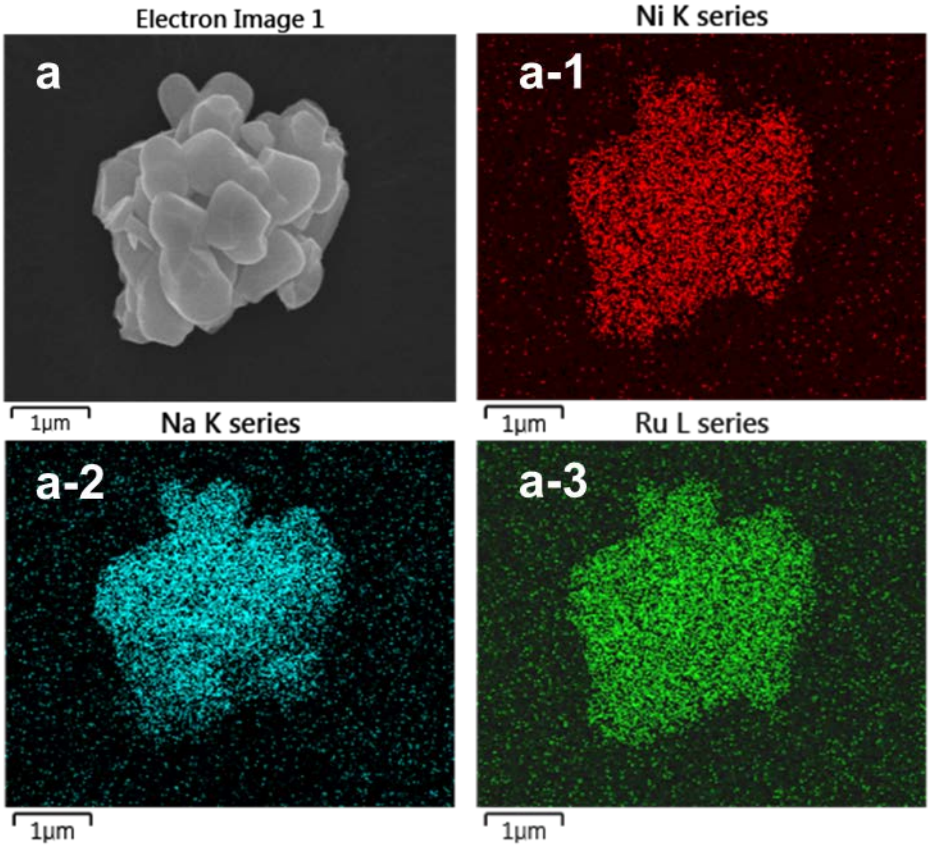

Figure S1. (a) SEM image and (a-1-a-3) EDX mapping of Na[$Ni_{2/3}Ru_{1/3}$]O_2.

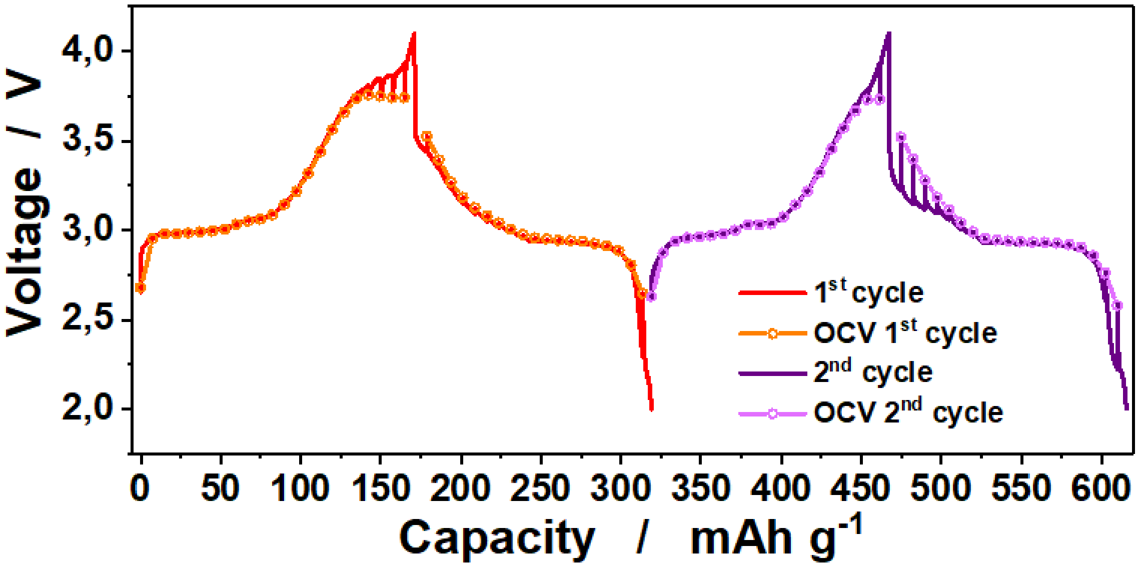

Figure S2. Comparison of GITT pitting curves and open-circuit voltage (OCV) of the $Na[Ni_{2/3}Ru_{1/3}]O_2$ electrode during first and second cycle.

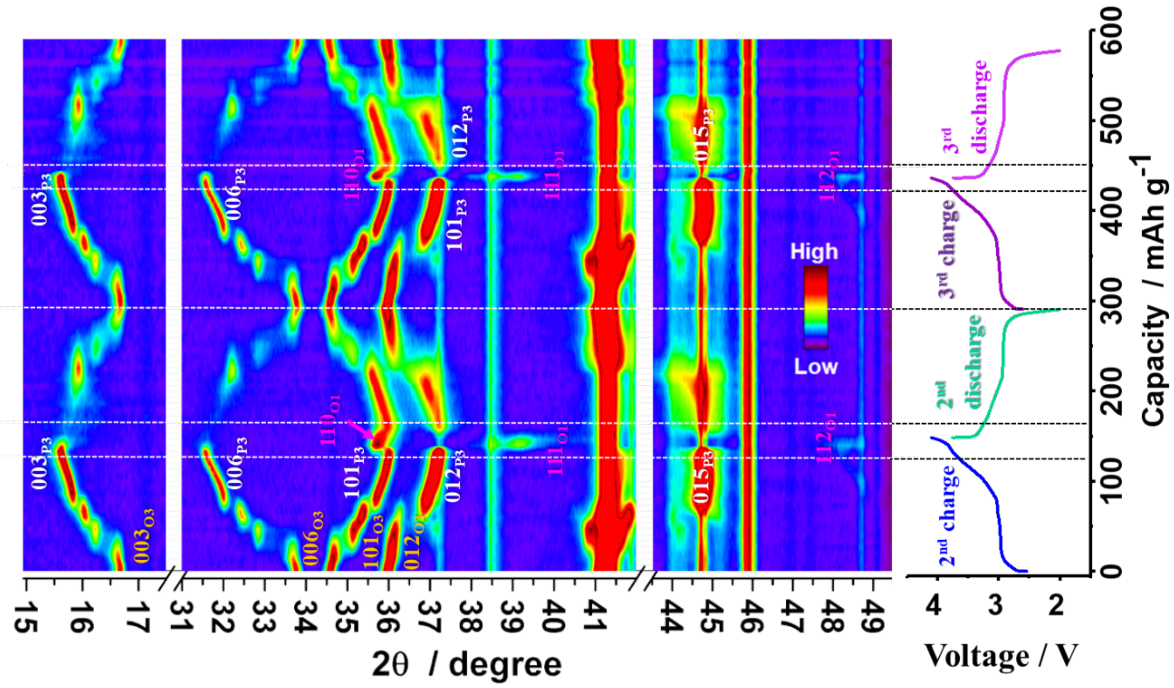

Figure S3. 2D image of *operando* XRD data of Na[$Ni_{2/3}Ru_{1/3}$]O_2 during the second and third cycles.

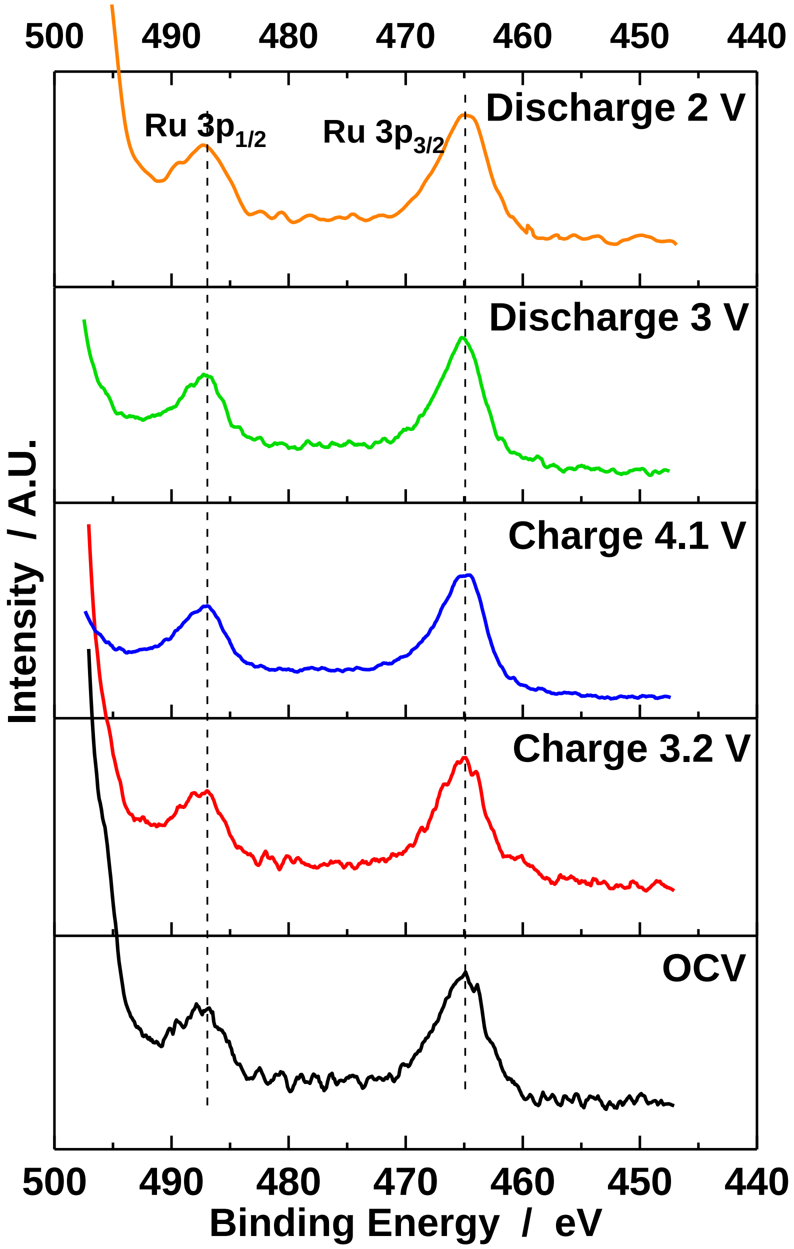

Figure S4. XPS spectra of Ru 3*p* for OCV, charged to 3.2 V, charged 4.1 V, discharged to 3 V and discharged to 2 V Na[$Ni_{2/3}Ru_{1/3}$]O_2 electrodes.

Table S2. Comparison of oxidation states of Ru in different layered materials.

Composition	**Phase**	**Oxidation state**	**Redox couples**	**Reference**
$Na[Ni_{2/3}Ru_{1/3}]O_2$	O3 ($R\bar{3}m$)	Ru^{5+}	inactive	[43]
$Na[Mg_{2/3}Ru_{1/3}]O_2$	O3 ($R\bar{3}m$)	Ru^{5+}	Ru^{4+}/ Ru^{5+}	[42]
Na_3RuO_4	O3 (C2/m)	Ru^{5+}	inactive	[47]
$Na_{0.66}Li_{0.22}Ru_{0.78}O_2$	P2 ($P63/mmc$)	Ru^{4+}	Ru^{4+}/ Ru^{5+}	[34]
$Na_2Ru_{0.95}Zr_{0.05}O_3$	O3 (C2/c)	Ru^{4+}	Ru^{4+}/ Ru^{5+}	[48]
$Na_{0.88}Cr_{0.88}Ru_{0.12}O_2$	O3 ($R\bar{3}m$)	Ru^{4+}	inactive	[49]
$Na_{0.75}Ni_{1/3}Ru_{1/6}Mn_{1/2}O_2$	P2 ($P63/mmc$)	Ru^{5+}	inactive	[46]
Our $Na[Ni_{2/3}Ru_{1/3}]O_2$	O3 ($R\bar{3}m$)	Ru^{5+}	inactive	Current work

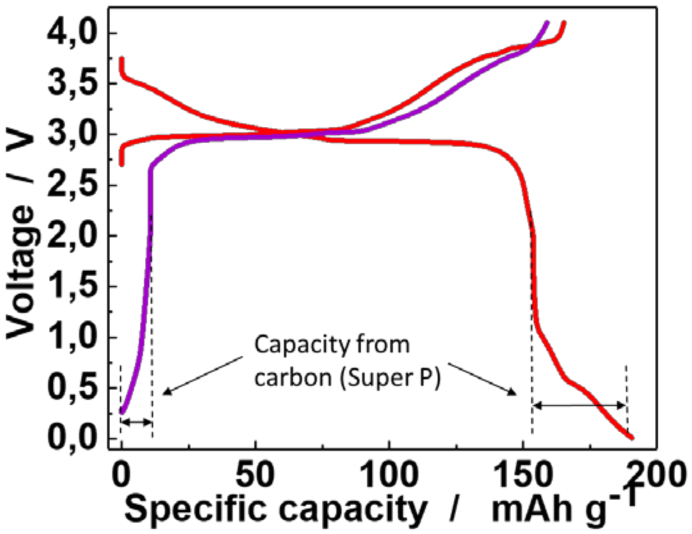

Figure S5. Charge and discharge profiles of Na[$Ni_{2/3}Ru_{1/3}$]O_2 tested in the voltage range of 0–4.1 V at a current of 0.05C.

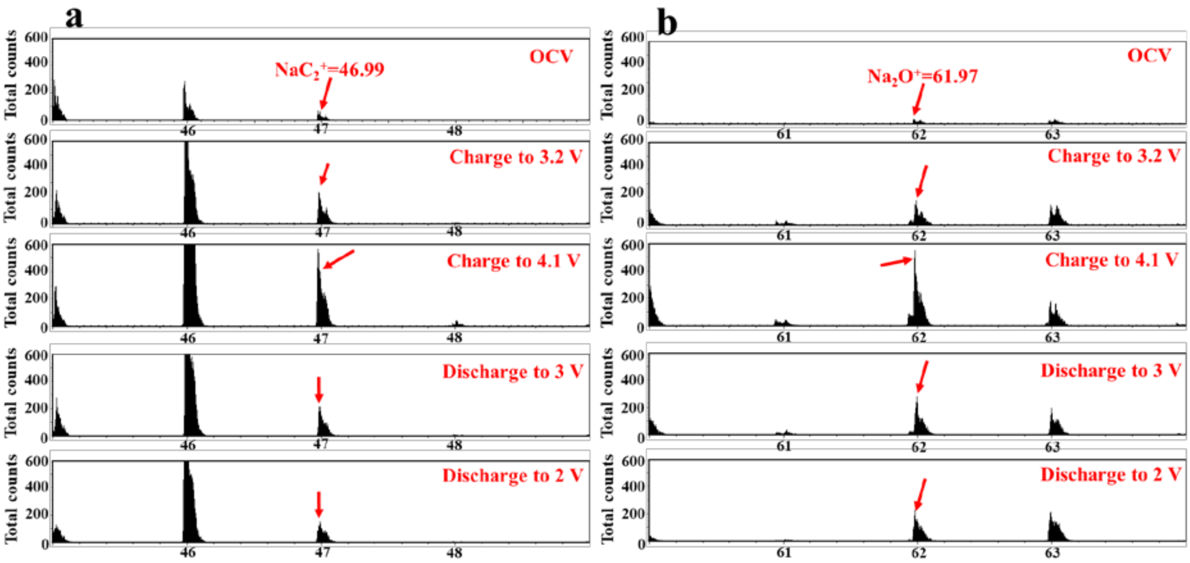

Figure S6. TOF-SIMS spectra of the (a) NaC_2^+ positive fragment (*m*=46.99) and (b) Na_2O^+ positive fragment (*m*=61.97).

Table S3. Comparison of performance of reported oxygen-redox-based O3-type cathode materials for sodium-ion batteries

Material	**Average operation voltage / V**	**Discharge capacity / mAh g^{-1}**	**Energy density / Wh kg^{-1}**	**Reference**
Na_2RuO_3	2.8	140	392	[38]
$Na_{0.6}Li_{0.2}Fe_{0.4}Ru_{0.4}O_2$	2.5	80	200	[50]
$Na_2Ru_{0.9}Mn_{0.1}O_3$	2.5	155	387.5	[55]
$Na_2Ru_{0.75}Sn_{0.25}O_3$	2.8	145	406	[40]
$NaMg_{0.67}Ru_{0.33}O_2$	2.8	84	235.2	[42]
$Na_{1.2}Mn_{0.4}Ir_{0.4}O_2$	2.5	135	337.5	[51]
Na_2IrO_3	2.7	130	351	[41]
$Na[Li_{1/3}Mn_{2/3}]O_2$	2.6	190	494	[56]
$Na[Ni_{2/3}Ru_{1/3}]O_2$	**3.02**	**154**	**465**	**Current work**